Modeling and Identification of Peripheral Artery Behavior and Systemic Hemodynamics using Non-invasive Wearable Sensors

by

Lu Wang

A dissertation submitted in partial fulfillment
of the requirements for the degree of
Doctor of Philosophy
(Mechanical Engineering)
in the University of Michigan
2020

Doctoral Committee:

Professor Kenn R. Oldham, Chair
Associate Professor Eric Johnsen
Professor Kayvan Najarian
Assistant Professor Bogdan Popa

Lu Wang
wangluhy@ umich.edu
ORCID iD: 0000-0003-2337-2619

DEDICATION

I dedicate this dissertation to my wife Yun Han, for all her love and support.

ACKNOWLEDGMENTS

This dissertation work would not have been possible without help, support, and encouragement from many great individuals. First and foremost, I owe my deepest gratitude to my advisor, Professor Kenn Oldham, for his guidance, persistent help and encouragement. His enthusiasm, creative thinking, efficiency in work deeply influence me. I am so fortunate to be able to have his guidance throughout my graduate studies. I appreciate that he always makes himself available, genuinely cares about his students, and trust his students. I appreciate all the work that he has done to help me grow and move to the next stage of my career. I would like to sincerely thank my committee members: Professor Eric Johnsen, Professor Kayvan Najarian and Professor Bogdan Popa. They have always given me constructive comments and suggestions. Their guidance and knowledge are the most valuable resource I have on campus.

I also want to thank the colleagues at the Michigan Center for Integrative Research in Critical Care (MCIRCC). I am particularly grateful for the assistance given by Dr. Sardar Ansari for his thoughtful suggestions and great help on clinical experiments. I would like to thank Dr. Kevin Ward, Dr Hakam Tiba and Brendan McCracken for their firm support and substantial help.
I am truly blessed to have many fantastic friends and loving family members in my life. I feel so lucky that I can share my thoughts, worries and happiness with my dearest friends. They always stand by me in my difficult times. Also, I would like to express the deepest appreciation to my parents, Wanmao Wang and Linxin Yang. I thank my patients for their endless love, support and trust. I would not accomplish my degree without their support and encouragement.

Finally, and most importantly, I thank my wife Yun Han. Thank you for being with me for ten years, listening to me, inspiring me, taking care of me and sharing your life with me. Having you by my side is the best thing in my life. Your love makes my life so special and beautiful.

TABLE OF CONTENTS

LIST OF FIGURES

LIST OF TABLES

ABSTRACT

The state of the peripheral arteries is known to be a key physiological indicator of the body's response to both acute and chronic medical conditions. For example, the body's vascular tone, or constriction of the arteries relative to a maximally dilated state, is a direct indicator of the body's response to cardiovascular stress. However, vascular tone is very difficult to assess using existing technologies, especially noninvasively. Peripheral arterial constriction or dilation is also the dominant factor in determining the body's systemic vascular resistance (SVR), or resistance felt by the heart in forcing blood through the circulatory system, and vascular resistance change is a major means of compensation to maintain physiological homeostasis. Situations where rapid changes in vascular tone and SVR are known to have great importance include shock (septic, cardiac, traumatic, etc.), post-surgical recovery, and hemodialysis.

The candidate proposed a technique for tracking changes in vascular tone by combining a photo plethysmography sensor with an adjacent compliant piezoelectric polymer pressure sensor (polyvinylidene fluoride). A simple local model for viscoelastic dynamic behavior of the underlying artery and surrounding tissue is generated and coupled to the piezoelectric sensor model, from which variations in relative amplitude and hysteresis between the piezoelectric and photo plethysmograph signals are found to show strong correlations with invasively measured SVR data in swine subjects. The mean absolute percentage errors were less than 4.7% and root mean square errors were less than 0.037 for all three swine subjects.

A local nonlinear artery model with extended Kalman filter performed system identification and tracking of the radius of the peripheral arteries as well as blood pressure. In proof-of-concept testing on a swine test subject, local vascular resistance calculated from arterial radius estimates at the ring location showed good agreement with overall systemic vascular resistance, with a 2.7% mean absolute percentage error and 0.026 root mean square error, while capturing other features of local cardiovascular behavior more noisily. Further validation is performed with ultrasound measurements of foreleg arterial radius while measurements with compliant sensors are taken.

Additionally, the candidate introduced a new systemic hemodynamic model, combining vascular resistance with heart rate, which may provide substantial insight into cardiovascular response to clinical interventions. This work attempted to better understand how estimated changes in local peripheral arterial radius obtained from wearable sensors relate to dynamic compensation in the full cardiovascular system. Preliminary human study results show that hemodynamic decompensation can be predicted under criteria based on peripheral vascular resistance from local EKF estimations and systemic hemodynamic feedback model error. Under the certain criteria, sensitivity to future decompensation was 100% and specificity was 88% for the training data set, and 100% and 84% for the full 50 patient sample.

Chapter 1 Introduction

1.1 Cardiovascular System and Peripheral Arterial Condition

The cardiovascular system can be thought of as the transport system of the body. This system has three main components: the heart, the blood vessels and the blood itself. The heart is the system's pump and the blood vessels are its delivery routes. Blood can be thought of as a fluid which contains the oxygen and nutrients the body requires and which carries the wastes the body needs to remove. The following terminology describes the structure and function of the heart and the cardiovascular system as a whole. The cardiac cycle is the sequence of events that occurs in one complete beat of the heart. The pumping phase of the cycle, also known as systole, occurs when the heart muscle contracts. The filling phase, which is known as diastole, occurs when the heart muscle relaxes.

Cardiovascular intensive care refers to special systemic management for those patients with severe cardiovascular disease (CVD), which consists of heart disease and vascular disease. CVD is one of the leading causes of death in the world [1]. In order to reduce deaths due to CVD, intensive care units for severe CVD patients, the so-called cardiovascular intensive care unit (CICU), have been developed in many general hospitals. Technological developments of clinical cardiology, such as invasive hemodynamic monitoring and intracoronary interventional procedures and devices, have resulted in evolution of intensive care for CVDs. As a result, severe CVD patients admitted to CICU are increasing year by year. It is necessary for optimal patient care to select effective means from various hemodynamic tools and to adjust the usage according to the clinical situation such as cardiogenic shock [2] and acute heart failure[3]. Furthermore, the patients in the CICU often have various complications such as respiratory failure and renal failure [4].

The state of the peripheral arteries is known to be a key physiological indicator of the body's response to both acute and chronic medical conditions. For example, the body's vascular tone, or constriction of the arteries relative to a maximally dilated state, is a direct indicator of the body's

response to cardiovascular stress. However, vascular tone is very difficult to assess using existing technologies, especially noninvasively. Peripheral arterial constriction or dilation is also the dominant factor in determining the body's systemic vascular resistance (SVR), or resistance felt by the heart in forcing blood through the circulatory system, and vascular resistance change is a major means of compensation to maintain physiological homeostasis. Situations where rapid changes in vascular tone and SVR are known to have great importance include shock (sepsis, cardiac, traumatic, etc.) [2] [3], post-surgical recovery [5] [6], and dialysis [4], in addition to relevance to CVD.

Despite the potential value of being able to continuously and rapidly monitor vascular tone and SVR, existing technology for acquiring this information is severely limited, especially using non-invasive technologies. Peripheral artery diameter can be directly measured only through biomedical imaging, typically ultrasound [7] [8], which is not available on a continuous basis or in most care settings. Acoustic techniques have also been proposed for measuring SVR [9]. The gold standard for SVR measurement is invasive monitoring of cardiac output, central venous pressure, and arterial pressure through catheterization, available only in intensive care settings, and not universally even then. Researchers have also proposed improvements on vascular resistance measurements by applying more complex models to aortic flow data [10] [11]. Non-invasive systems for estimating cardiac output, and from there inferring SVR, have been commercialized based on electrical cardiometry [12] and whole body bioimpedance [13]. However, these track SVR only weakly [14, 15], since central venous pressure is not measured, and are also unavailable outside of acute medical care settings.

Researchers have thus pursued methods for estimating SVR and vascular tone using simpler instruments. Prior attempts have generally relied on photo plethysmography (PPG) data, which tracks changes in artery volume within short-term pulse cycles. Timing of reflection waves as extracted from PPG data has been reported to indicate changes in peripheral arterial resistance, but this was only verified through basic correlations with expected trends among hypertension subjects, not individualized tracking [16]. Methods for extracting SVR from multiple regression of PPG waveform data points have been derived by machine learning techniques, but SVR estimation error ranged from 15%-100% for most subjects [17] [18]. Evaluating a vascular tone index by matching models for arterial dynamics to pulse transit time (PTT) and blood pressure (BP) measurements has also been proposed [19]. However, results could at most be correlated

with risk factors for high SVR, rather than SVR itself. Another report showed PTT correlation with SVR over time, but only for two individual cases [20]. Estimates of cardiac output and vascular resistance have also been suggested based on ECG and BP cuff data, and used in tracking response to physical activity, but these are recognized as only approximate measures [21].

Table 1 Existing techniques for measuring vascular tone and SVR are either highly specialized to intensive care settings, non-continuous, or limited in accuracy due to types of sensing available.

Quantity of Interest	Prior Techniques	Advantages	Limitations
Peripheral vascular tone (relative dilation or contraction of artery)	Ultrasound + Flow Mediated Dilation	Closest to a gold standard, agrees with measures of closely related variables.	Requires specialized equipment and expertise, non-continuous measurement.
	Arterial Tonography + Cuff reference	Absolute volume change available using pressure reference.	Specialized hardware, non-continuous measurement; testing requires pumps for pressure reference and cuff occlusion.
	PPG amplitude + Flow mediated dilation	Simplified sensing elements	Testing requires pumps for pressure reference and cuff occlusion.
	PPG + time reflective index	Readily available hardware, simple methodology.	Low resolution for reflective wave timing using PPG leads to weak correlation with other measures.
	PPG + Pulse transit time (PTT)	Conceptually feasible with wearable sensors.	Very limited validation, dependent on assumptions regarding arterial properties.
Systemic Vascular Resistance (SVR)	Pulmonary arterial catheter	Gold standard, gives central pressure and cardiac output.	Invasive, available only in intensive care setting, possibly slow response time.
	Electrical cardiometry (also: Whole body impedance)	Non-invasive, commercially available.	Available only in specialized clinical settings, correlation with conditions can be weak.
	PPG Waveform Analysis	Readily available hardware.	Weak correlation with invasive measures
	Wearable BP band + ECG	Continuous monitoring, even during physical activity	Uncalibrated, known to provide only rough measurement of systemic quantities (i.e. cardiac output, SVR).

1.2 Non-invasive Wearable Devices

Wearable versions of blood pressure cuffs, PPG sensors, and ECG sensors all exist commercially or as research systems, and pulse transit time has been extracted from both combinations of these

sensors or dedicated sensing elements. PPG data was heavily used in most prior studies because it has traditionally been one of the few non-invasive sensing techniques providing continuous time series data on cardiovascular function. But, due to issues such as electronic drift and ambient light sensitivity, a PPG can only directly measure relative change in volume within pulse cycles. Longer-term absolute changes in mean artery volume or diameter over minutes or hours must be inferred from features of the waveform or correlation with other vital signs. However, PPG resolution and signal complexity are also limited in most circumstances due to heavy filtering required to extract volume information by optical methods. Some of these limitations can be compensated for during vascular tone monitoring by adding a reference pressure and directly perturbing peripheral blood flow with a pressure cuff, but this reintroduces complexity to these systems and prevents continuous monitoring.

Attempts to perform vascular tone and/or SVR measurements non-invasively form a subset of efforts to acquire cardiovascular information from compact, wearable devices. A number of commercial and research systems provide estimates of heart rate and systolic and diastolic blood pressure. Nonetheless, these systems remain relatively large in size, and attempt to suppress intervening tissue dynamics to obtain interior pressure waveforms as accurately as possible.

Given the desirability of extremely compact cardiovascular monitoring, several researchers have developed much smaller, continuously wearable pressure transducers for use at peripheral arteries. The candidate's research group, for one, have developed a sensor based on a piezoelectric polymer (polyvinylidene fluoride, or PVDF) in a polymer laminate, designed to approximately match the compliance of tissue and arteries in a human finger. PVDF films were likewise previously used for waveform monitoring at the human wrist by Sur et al. [22] and for pulse and respiration monitoring at the chest by Chiu et al. [23] Even smaller sensing elements have been proposed based on thin-film lead-zirconate-titanate (PZT) in a polymer film [24], nanowire-impregnated polymers [25], and amorphous PZT films [26].

These sensor technologies have in common:

1. Sufficient compliance to deform with arteries and tissue, which can accentuate effects of changing arterial properties and/or dimensions.
2. High sensitivity to pressure variations, giving highly-detailed peripheral pressure waveforms.
3. Much smaller volume, weight, and power requirements than existing technologies, beneficial for long-term cardiovascular monitoring and ease-of-use in a wide variety of setting.

In contrast, this class of sensing technology lacks the ability to obtain absolute pressure measurements if no external reference (i.e. pressure cuff) is available. The influence of intervening tissue also distorts pressure waveforms compared to their profile inside the artery. However, these latter effects can potentially prove useful for monitoring tone, as this proposed work will examine.

1.3 Homeostatic Mechanisms and Cardiovascular System Feedback

The human body uses multiple mechanisms to maintain cardiovascular hemostasis. The baroreflex reflex is one of the body's homeostatic mechanisms. It helps to maintain blood pressure at nearly constant levels, by providing a rapid negative feedback loop in which an elevated blood pressure reflexively causes the heart rate to decrease and also causes blood pressure to decrease. Decreased blood pressure decreases baroreflex activation and causes heart rate to increase and to restore blood pressure levels [27]. Baroreflex adjustments are key factors in dealing with postural hypotension, the tendency for blood pressure to decrease on standing due to gravity.

The human body also regulates blood pressure and fluid and electrolyte balance, as well as systemic vascular resistance, by the renin–angiotensin system (RAS) [28]. While the baroreceptor reflex responds in a short-term manner to decreased arterial pressure, the RAAS is responsible for more chronic alterations. It is composed of three major compounds: renin, angiotensin II, and aldosterone. These three compounds act to elevate arterial pressure in response to decreased renal blood pressure, decreased salt delivery to the distal convoluted tubule, and/or beta-agonism. Through these mechanisms, the body can elevate the blood pressure in a prolonged manner, on time scales of hours to days.

Meanwhile, compensatory dynamic and system model of the cardiovascular system have been studied by various researchers. As an example, a theory and model relating pulse transit time (PTT) and blood pressure to changes in arterial dynamics have been developed [29]. Another example, intended to infer baroreflex feedback mechanisms, has also been proposed through a more detailed 3D–0D model [30]. Black box modeling of dynamics at various time scales, using similar identification techniques as this work, was reported in [31]. A set of low-order feedback dynamics with parameters identified from non-invasive measurement was previously proposed in [32], without measurements of vascular resistance.

1.4 Scope of Proposed Work

Our primary hypothesis is that arterial and tissue nonlinearities and dynamics that complicate standard blood pressure monitoring with wearable sensors can, in fact, be beneficial for tracking changes in vascular tone or SVR, in particular when combining information from multiple sensing modalities. Specifically, we propose to use a custom, miniature piezoelectric pressure sensing ring in combination with conventional PPG sensing. We will combine time series information provided by these sensors with local mechanical models for static and dynamic artery and sensor behavior. Taking advantage of phenomena characteristic of external pressure sensing with a compliant sensor, and by applying appropriate parameter identification algorithms, we believe that it will be possible to extract reliable information about changes in diameter of the underlying artery, as a continuous monitoring system for vascular tone.

Research Task 1: Assess peripheral artery behavior using non-invasive sensing methods

Non-invasive methods for measuring peripheral artery behavior have been proposed by several methods. Commercialized systems for estimating cardiac output, and then inferring SVR, have been developed based on electrical cardiometry [12] and whole body bioimpedance [13], but with weak SVR tracking performance due to lack of venous pressure information [14, 15]. Other studies have relied on pulse plethysmography (PPG), which tracks short-term changes in artery volume, by observing changes in timing of reflection waves in arterial flow [17] or applying multiple regression models, but accuracy of these approaches has been limited due to relatively low feature resolution in PPG waveforms[18]. Pulse transit time (PTT) has also been proposed for evaluating vascular tone [19], but to date these methods have either been validated only in comparison to risk factors for high SVR, rather than changing SVR over time, or documented for a very small number of patients [20].

Meanwhile, arterial dynamics of the cardiovascular system have been studied by various researchers. As an example, a theory and model relating pulse transit time (PTT) and blood pressure to changes in arterial dynamics were developed in [7]. Some researchers use simple linear or nonlinear constitutive equations to describe the pressure/cross-sectional area relationship [8][9][11], although more complex models are available [10]. Sherwin et al. [11] also included the effect of vessel tapering by considering a varying initial cross-sectional area of the vessel. Vessel collapse was specifically modelled in [9] by adapting the vessel properties and considering pressure changes in the collapsed vessel area. Ghasem et al. [17] proposed a model

with constant cuff pressure to estimate the central aortic BP waveform from two pulse volume signals. Those and other such models illustrate the importance of both longitudinal and radial behavior in interpreting arterial motion.

We first propose a method for estimating peripheral arterial radius by combining a PPG sensor with a compliant piezoelectric polymer (polyvinylidene difluoride, or PVDF) pressure sensor, worn as a ring or band about the artery being monitored (Chapter 2). Chapter 3 then focuses on use of the PPG and PVDF sensors to form a type of input-output relationship across a simple dynamic model for local deformation of the artery and other tissue. A local model for viscoelastic dynamic behavior of the underlying artery and surrounding tissue is generated and coupled to the piezoelectric sensor model, from which variations in relative amplitude and hysteresis between the piezoelectric and PPG signals are found to show strong correlations with invasively measured SVR data in animal subjects (swine). Arterial radius is introduced as an augmented state in an extended Kalman filter, with the Kalman filter then used to perform system identification and tracking of relative changes in arterial radius over time.

In Chapter 4, the model is expanded to account for the most prominent longitudinal features of interaction between underlying tissue and the compliant piezoelectric sensor. We propose a 2-D model for arterial blood pressure, volumetric flow rate and artery radius with a varying outside cuff pressure. Here, we attempt to incorporate limited longitudinal behavior with peripheral arterial contraction dynamics beneath the PVDF/PPG sensor assembly to interpret variations in sensor signal behavior at varying applied external pressure.

Research Task 2: Identify systemic hemodynamics with respect to peripheral vascular resistance.

Cardiovascular systems of both swine and humans feature several feedback mechanisms that aid in regulation of core blood pressure. Vascular resistance, or the resistance to fluid flow experienced by the heart, is considered one of the primary compensatory mechanisms in response to cardiovascular stress over short- to medium-term timeframes (seconds to hours) [2], managed largely through contraction or dilation of peripheral arteries [13]. However, these changes in peripheral arterial radius are difficult to monitor continuously, with imaging-based methods [7] available only on an intermittent basis, and indirect measurements based on metric such as pulse transit time or waveform analysis of PPG measurements having limited accuracy [17].

Here, we expect tracking vascular resistance in combination with heart rate can provide substantial insight into cardiovascular response to clinical interventions, at least under very controlled circumstances. A new systemic hemodynamic model be able to reproduce oscillatory trajectories that appear to arise from different timescales of response to medication, and identifiable changes in the system.

Research Task 3: Predict hemodynamic decompensation with the systemic model

The body's ability to compensate against stress caused by trauma, illness, and disease can substantially complicate diagnosis and detection of complications in many situations. For example, multiple autoregulatory feedback loops exist to maintain sufficient blood pressure at the core and vital organs. As a result, measurements of blood pressure tend to act as a trailing indicator of distress, while feedback behaviors that are much more difficult to monitor may be changing rapidly. Thus, early prediction of hemodynamic decompensation, or a rapid decrease in blood pressure, has remained difficult to achieve, due to limitations on physiological monitors and patient-to-patient variability.

One clinical situation in which hemodynamic decompensation is relatively common is during hemodialysis. Several prior studies have attempted to predict when IDH will occur, either by classifying patient risk factors prior to hemodialysis [33] or applying statistical and/or machine learning techniques to existing physiological measures taken during hemodialysis, such as blood pressure (BP) trends, the electrocardiogram (ECG), pulse photoplethysmogram (PPG), and/or heart rate variability (HRV) data [34] [35] [36] [37] [38]. However, sensitivity and specificity of these predictors remains limited.

Here, we hypothesize that incorporating peripheral vascular resistance into feedback models for cardiovascular autoregulation can further increase understanding of decompensation and improve IDH prediction. This differs from previous attempts to model feedback dynamics primarily in the availability of additional feedback signals from non-invasive sources, and also the examination of variation in feedback over time during the complex medical intervention of hemodialysis.

Chapter 2 Sensor Description

2.1 Piezoelectric Sensor Design

This chapter describes the sensing apparatus used to collect data from animal and human subjects over the course of this work. The basic sensor designed for this work transforms mechanical stress, produced from the pulse in the artery, into an electrical signal. It can be placed over arteries that are easy to access, such as those in the wrist, finger, ankle, foot, temple, etc. The digital arteries in the finger were chosen as the location for this work because they allow a detailed pulse to be captured by the sensor with little intervening tissue. Therefore, the sensor is designed to fit a in a ring that could contact both arteries in the proximal or middle phalanx part of the middle or index finger, and to be compliant with certain hospital requirements.

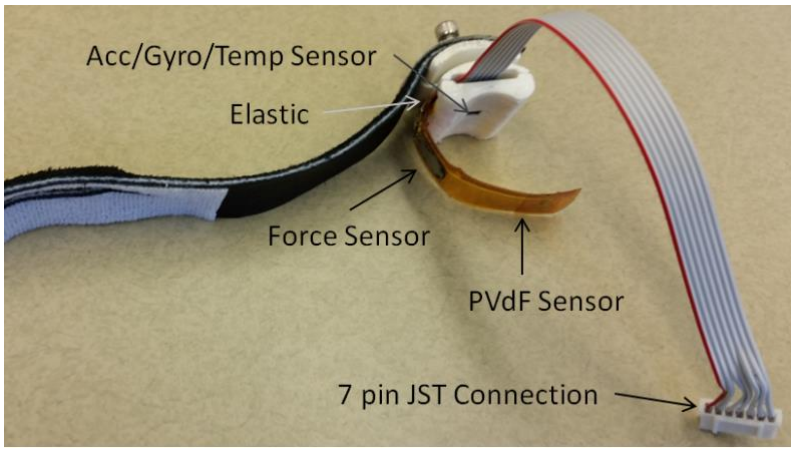

Fig. 1 Finger cuff ring and flexible sensor components.

2.1.1 Engineering Specifications

Ring requirements, based on conversations with clinicians and early testing on human volunteers, are summarized as follows:

- The sensor should fit on standard middle or index finger, with radius of approximately 9 mm and width of approximately 20 mm.

- The sensor should deform and experience stress in the sensing material with each pulse.
- A ground circuit should be present with contact to skin to reduce noise.
- The sensor should meet hospital standards for materials.

2.1.2 Material Selection

Piezoelectric materials were chosen as the transduction material in the sensor for their electro-mechanical properties, which transform the mechanical deformation created by the pulse into an electrical signal that can be read by circuitry. Two piezoelectric materials were compared Polyvinylidene fluoride (PVDF), which is a thin polymer film, and lead-zirconate-titanate (PZT), which is a hard ceramic. It was assumed that the stress applied to the sensor would be similar to a compression force in the radial direction of the ring and/or of the hoop stress in a thin walled pressure vessel, due to the change in volume of the finger created by the artery pulse. This change results in a change in pressure that creates stress in the tangential direction.

Both cases were examined using that electro-mechanical coupling factor, which compares a material's piezoelectric constant for stress in a specified direction and dividing it by the relative dielectric constant. The PVDF was also considered easier to use in manufacturing and considered to be more durable then the PZT; as PZT elements tested were made from a thin ceramic, durability came into question during initial testing, often cracking when the ring was tightened to adjust pressure.

A polyimide film, known as Kapton tape, was chosen to create a laminate around the PVDF film due to its chemically resistive and electrical insulating properties, ability to be used over a wide range of temperatures, small thickness (25.4 μm), durability, and Young's modulus over three times smaller than PVDF, allowing for more stress to be applied to the sensing layer.

Table 2 Sensor materials

Item	Part	Manufacturer	PN	Supplier
1	PVdF 52 micron uniaxially stretched poled with gold on chrome electrodes on both sides	Precision Acoustics	PV52G	Precision Acoustics
2	1 Mil Kapton tape 0.5 '' (polyimide film)	Kapton tape	KPT-1/2	Kapton Tape
3	Silver epoxy	MG Chemicals	8331S-15G	Digikey
4	Flat cable, 28 AWG, 0.05'' Pitch	3M	3365/09 100SF	Digikey
5	Copper Tape	3M	1181 X 1/4"	Digikey

The original sensor size of 50mm by 9mm was chosen to maximize its area of contact on the finger and for ease of construction with the Kapton tape. Through experimental testing it was determined that this was too large, making it difficult to put the sensor on many subjects due to its length. Thereafter it was shortened to 40mm. The PVDF film was placed between protective layers of polyimide tape (Kapton Tape, Uline Inc.), which was then worn under a Velcro or elastic band. A set screw element allows adjustment of the sensor to a relatively consistent level of tension. The sensor is shown applied to a sample swine subject in Fig. 2. Dedicated sensing circuits and a data-logging microcontroller are available, or the sensors can be connected directly to commercial biomedical data acquisition systems (e.g., DA100C, BIOPAC Systems Inc.), with the latter being used to acquire data presented in this work.

An exploded view of the primary sensor model used in this work is Shown in Fig. 1, showing locations of key components. A detailed manufacturing procedure is provided in the appendix.

2.3 Wearable Finger Cuff Ring Design

For the sensor to work properly it needs to be held in place at the correct position and with modest pre-pressure that allows it to deform with the pulse from the arteries. We also had interest in integrating several components into its design that might be useful for long term stability, including pressure and temperature sensors and a 6 axis accelerometer/ gyroscope. These are expected to be used to develop methods to refine signals and improve artifact interpretation, though such features have not been implemented at this time. The full assembly is again intended to fit over the proximal phalanx of the middle or index finger holding the sensor in place. The assembly is also used to adjust the pressure between the sensor and finger.

A ring was also designed to house and properly position all of these components, and would later be modified to create a wristband version that could be used for specialized research experiments. Control of applied pressure is obtained by separating two plates using a screw. The screw is attached to the top plate and when rotated down pushes on the bottom plate decreasing the volume inside the ring and increasing the pressure. Therefore, by adjusting the screw the pre-pressure on the ring can be adjusted to find the optimal signal clarity from the sensor for each patient.

Cloth and leather were chosen for strap material based on empirical testing, because they allowed more details and larger signal output then the other materials that were considered. These included solid aluminum backing, copper tape, foam, nylon and elastics.

A FlexiForce A301 Sensor, rated for 4 Newtons, was evaluated for reading of absolute pressure applied to the finger, based on a predicted pressure of 10 to 16 kPa or 1 to 2 newtons of force under sensor operating conditions. However, both the FlexiForce and a second candidate force sensor (Interlink 400 Short Tail) were found to be unstable at the forces being measured. This meant that reference pressure applied to at the ring is not known in most experiments, though work described in Chapter 6 will help explain why consistent behavior could be obtained across subjects without this information.

2.4 Flexible Piezoelectric and Photoplethysmography Sensor Design

During the majority of the work described in this thesis, we used the custom-built flexible piezoelectric sensor described in Section 2.3 with the ring assembly described above for acquiring pressure signals during vascular resistance tracking, together with a separate off-the-shelf PPG sensor (OXY200 and BioNomadix, BIOPAC Systems Inc.). However, a second-generation sensing ring was also developed incorporating a PPG directly with the piezoelectric sensor, shown in Fig. 2 . The ring again consists of a polymer laminate with a piezoelectric PVDF sensing layer (52 μm thick, silver plated, Precision Acoustics), with an additional flexible printed circuit board on which to mount the PPG sensor (SFH 7050).

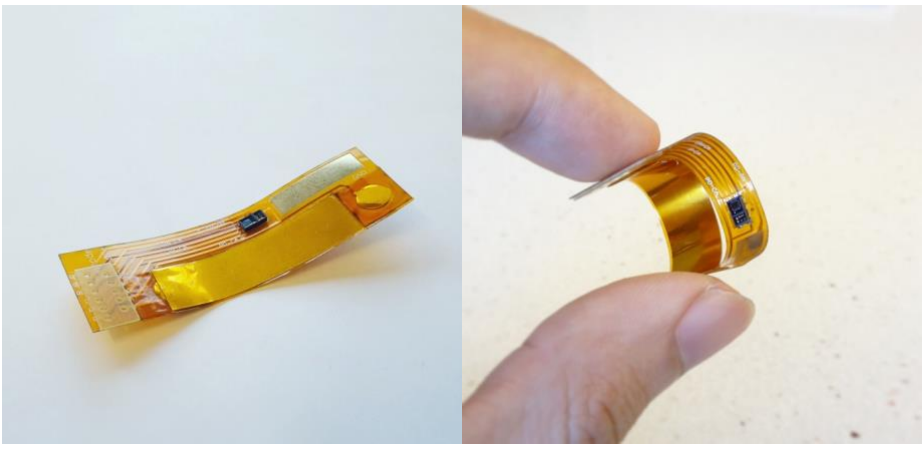

Fig. 2 Compliant polyvinylidene fluoride (PVDF) piezoelectric sensing band for non-invasive artery monitoring

A sample time response of the piezoelectric sensor on the foreleg of a swine subject over three cardiac cycles is shown in Fig. 4a. The unprocessed response of the piezoelectric sensor can be considered as approximately the time derivative of pressure at the site, with this differentiation resulting from the input impedance of the piezoelectric element. However, the signal is further mediated by tissue and artery motion as they interact with the compliant sensor, in addition to some electrical filtering; as a result, integration of the signal (Fig. 4b) returns a similar but not identical waveform to non-invasive blood pressure measurements (CNAP Monitor, CNSystems Medizintechik AG), in which feedback control holds artery volume constant, or to invasive arterial lines. PPG data from the same swine, shown in Fig. 4c, is comparatively less detailed, which has tended to impede its success in monitoring vascular tone in previous studies. However, as will be discussed, the difference in dynamics between PPG and piezoelectric pressure sensor measurements as they respond to changes in the internal artery may provide important information on artery status.

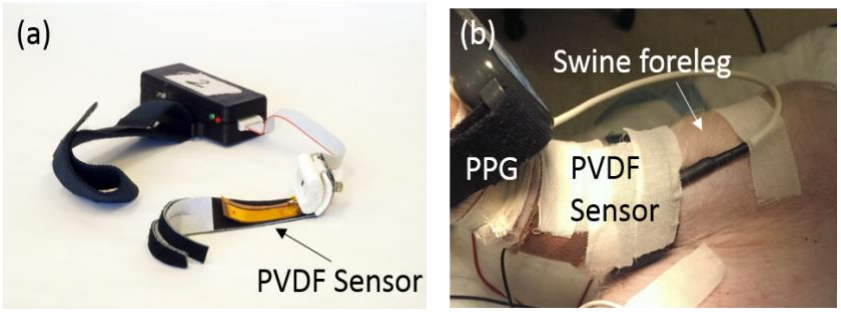

Fig. 3 (a)Example polyvinylidene fluoride (PVDF) sensor; (b) sensor applied to foreleg of swine test subject.

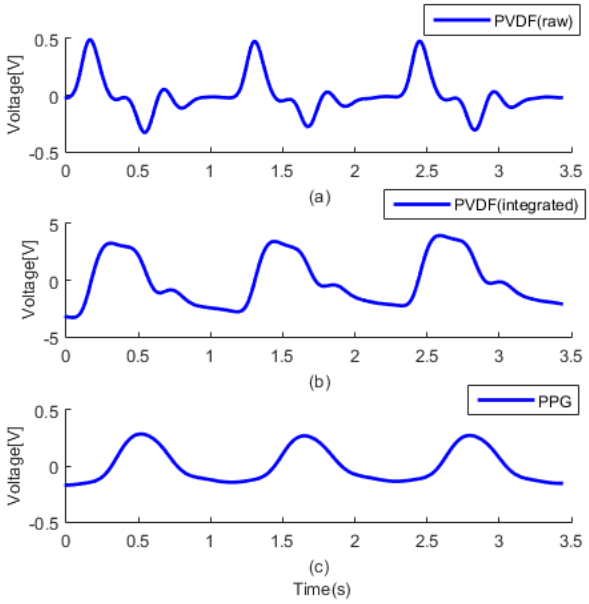

Fig. 4 Sample signals from swine subject of (a) compliant piezoelectric ring output; (b) Integrated piezo signal corresponding to fluctuations in pressure at tissue surface under ring; (c) PPG waveforms with less detail but alternate dependence on perturbation.

Chapter 3 Modeling of Peripheral Arterial Behavior

In this chapter, a model is derived to account for the most prominent features of interaction between underlying tissue and a compliant piezoelectric sensor. A simple local model for viscoelastic dynamic behavior of the underlying artery and surrounding tissue is generated and coupled to the piezoelectric sensor model, from which variations in relative amplitude and hysteresis between the piezoelectric and PPG signals are found to show strong correlations with invasively measured SVR data in animal subjects (swine)[39].

3.1 Pulse Plethysmograph (PPG)

The first sensor used in the proposed vascular resistance tracking scheme is a commercial PPG. In a PPG sensor, the change in artery volume is detected by illuminating the skin with the light from a light-emitting diode (LED) and then measuring the amount of light transmitted to a photodiode. A photodetector converts light energy into an electrical current, which connects to low noise electronic circuitry that includes a transimpedance (current-to-voltage) amplifier and filtering circuitry. A high pass filter reduces the size of the dominant DC component and enables the pulsatile AC component to be amplified. A low-pass filter is also used to remove the unwanted higher frequency noise such as electric interference (i.e. 60 Hz noise).

The voltage output of the PPG sensor is, ideally, proportional to the change of the artery's volume. However, due to the transimpedance amplification and need for high-pass filtering to obtain the time-varying component of light, PPG sensors do not provide long term tracking of mean absolute arterial volume, but rather respond to short term fluctuations in arterial volume during cardiac cycles. In effect, changes in volume are convoluted with amplifier and filter dynamics, which include a differentiation, then integrated to return the relative volume fluctuations. As a model, this becomes

$$U_{PPG} = K_{PPG} \int h_{PPG} * V_i dt = K_{PPG} \int h_{PPG} * \pi r_i^2 L_{PPG} dt \qquad (1)$$

where K_{PPG} is the gain of the PPG sensor, h_{PPG} is the a linear dynamic filter response, and V_i is volume of oxygenated blood between the LED and photodector, which can alternatively be related to the inner radius of the artery r_i and length of artery illuminated by the PPG, L_{PPG}. The length of the artery under PPG sensor is assumed to be constant. The exact filter in the PPG sensor is not disclosed by the manufacturer, but an approximate model was based on literature reports [27] in this work, and experimentally produced a response consistent with information from invasive sensors. The PPG filter model used was

$$H_{PPG}(s) = \frac{6s}{(s+2)(s+100)} \tag{2}$$

3.2 Piezoelectric Sensor: Electrical

The second sensor used was the piezoelectric PVDF pressure sensing ring. In the electrical domain, the piezoelectric sensor can be modeled as a charge source in parallel with the sensor's capacitance. A high impedance charge mode amplifier, such as the BIOPAC data acquisition system used in this work, converts electrical charge to voltage. To account for interface circuit dynamics, a custom-built electrical circuit was designed that provided comparable frequency response to the BIOPAC system. The sensing circuit must compensate for very low current from the PVDF sensor, measured around 1-5 nA. The nominal sensing circuit consists of a first stage amplifier, followed by a low pass filter that helps minimize electrical interference and high frequency noise. Large resistors were selected because low current signal and low capacitance of PVDF sensor, which decrease the high-pass filter cut-off frequency.

Charge on the PVDF sensor is given by

$$q = d_{31} E A \varepsilon_1 \tag{3}$$

where, q is the electrical charge between PVDF surfaces, E is the elastic modulus of PVDF, A is the surface area of the PVDF, and ε_1 is the tangential strain in the PVDF layer. In this model, compressive piezoelectric response (i.e. d_{11}) and coupling effects are neglected as small compared to the dominant response from hoop stress around the ring formed by the sensor.

Transfer function of Fig. 4 was used as a model for PVDF sensor circuit dynamics, which can be written as:

$$G(s) = \frac{18s}{(s+6)(s+178)} \tag{4}$$

The PVDF sensor output is a convolution of the time-varying charge with the amplifier dynamics, h_{pvdf}, to produce a voltage output, which in turn is integrated to obtain the final PVDF sensor response, U_{pvdf},

$$U_{ovdf} = \int h_{pvdf} * qdt = \int \frac{18s}{(s + 1/RC)(s+6)(s+178)} * qdt \tag{5}$$

where R and C is the impedance of the PVDF sensor and the equivalent capacitance, respectively. The integration is required because the small charge amplitude and relative impedance of the sensor result in a high-pass filter cut-off frequency much higher than the frequency of cardiac cycles; integration returns this to an output approximately proportional to blood pressure, but mediated by intervening tissue, as discussed below.

3.3 Piezoelectric Sensor: Mechanical

The piezoelectric sensor responds predominantly to tangential stress or strain in the PVDF ring as it stretches in response to fluctuations in pressure and volume inside the underlying arteries. However, the pressure experienced by the PVDF ring is not identical to the underlying arterial pressure, due to additional tissue dynamics. To approximate this behavior, a very simple mechanical model is used, that also supports dynamic modeling of viscoelastic effects seen to be important to artery and sensor behavior.

The mechanical model used in this work consists of a thick-walled cylinder for the artery including a nonlinear elastic modulus approximation, other soft tissue and skin approximated as a compressible volume, and a linear elastic ring approximation for the sensor, as shown in Fig. 5. The basic assumption of mechanical model is that the artery is straight and the cross-sectional property like tissue and bone are same along the width of PVDF sensors, which is 9mm. The peripheral artery is approximated using a linear thick-walled elastic tube model,

$$\frac{\delta r_i}{\bar{r}_i} = \frac{1}{E(r_i)}\left[f_{ii}(\bar{r}_i, \bar{r}_o)\delta p_i - f_{io}(\bar{r}_i, \bar{r}_o)\delta p_o\right] \tag{6}$$

$$\frac{\delta r_o}{\bar{r}_o} = \frac{1}{E(r_o)}\left[f_{oi}(\bar{r}_i, \bar{r}_o)\delta p_i - f_{oo}(\bar{r}_i, \bar{r}_o)\delta p_o\right] \tag{7}$$

Where $\bar{r}_i$ and $\bar{r}_o$ are the average inner and outer radius of the artery wall, δr_i and δr_i are their variation in time during a cardiac cycle, E is artery elastic modulus, δp_i is pressure change inside the artery, and δp_o is pressure change as experienced by the sensor, which may differ from δp_i due to internal stresses in the artery walls and compressibility of intervening tissue but is assumed to approximately isotropically resist arterial expansion. f_{ii}, f_{oi}, f_{io}, and f_{oo} are functions for circumferential stress at the inner (i) or outer (o) radius of the artery, as defined for a standard thick-walled elastic tube in [28].

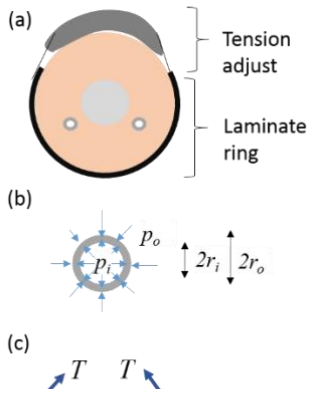

Fig. 5 (a) Schematic drawing of finger cross section with free-body diagrams of (b) artery with internal and external radii r_i and r_2 subject to internal and pressures p_i and p_o (c) and ring sensor with radius R under tension T constraining artery expansion under simplifying assumption of approximately isotropic pressure distribution under ring.

The piezoelectric sensor response is modeled as thin-walled cylinder subject to approximately uniform pressure from the underlying tissue (p_o) and an initial tension, T, in the sensor. Perturbations of the sensor radius, δR, from its nominal radius, $\bar{R}$ are modeled in the form

$$\delta R = \frac{2\bar{R}^2}{E_s t}\delta p_o - \frac{\bar{R}}{E_s t}\delta T \tag{8}$$

Where E_s is the composite modulus of the PVDF and polyimide layers, t is the sensor band thickness, and δT represents any external perturbations to tension in the sensor, though in this study T is generally held constant.

Interior artery expansion can be related to deformation of the sensor by a conservation of area or volume,

$$\pi\left(\bar{R}+\delta R\right)^2 = 2\pi\left(r_o+\delta r_o\right)^2 + V_o - \gamma\delta p_o \tag{9}$$

where V_o is the nominal cross-sectional tissue area enclosed by the sensor, excluding arteries, and γ is a measure of net intervening tissue compressibility. Two major arteries are known to be present under the appendage being monitored.

Combining (6)-(9) and assuming external tension, *T*, is fixed, a nonlinear function relating sensor pressure perturbations, δp_o to artery perturbations, δr_o, can be obtained:

$$\pi\left(\bar{R}+\frac{2\bar{R}^2}{E_s t}\delta p_o\right)^2 = 2\pi\left(r_o+\delta r_o\right)^2 + V_o - \gamma\delta p_o \tag{10}$$

3.4 Dynamic Effects

It is well known that both artery and skin exhibit viscoelastic behavior that leads to hysteretic behavior during phases of increasing versus decreasing pressure during cardiovascular cycles. Experimental comparison of the PVDF sensor response to blood pressure measurements using a finger cuff, in which pressure is regulated to maintain a constant arterial volume, show a clear hysteresis in piezoelectric signal, consistent with hysteresis arising from viscoelastic effects in tissue. To capture this behavior, a simple viscoelasticity model is added to the mechanical model from Section 3.C. The Standard Linear Solid Model, used here, combines Maxwell model dynamics and a Hookean spring in parallel to relate a stress, σ, to a strain, ε; a viscous material is

modeled as a spring and a dashpot in series, both of which are in parallel with a lone spring, as shown in Fig. 6.

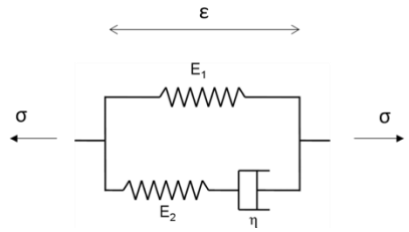

Fig. 6 . The Standard Linear Solid Model uses lumped spring and dashpot elements to relate stress, σ, to strain, ε, in a viscoelastic material using two parameters for elastic modulus, E_1 and E_2, and a viscoelasticity parameter, η.

For the model in Fig. 6, the governing constitutive relation is:

$$\frac{d\varepsilon(t)}{dt} = \frac{\frac{E_1}{\eta}\left(\frac{\eta}{E_2}\frac{d\sigma(t)}{dt} + \sigma(t) - E_1\varepsilon(t)\right)}{E_1 + E_2} \tag{11}$$

where σ is the applied stress, E_1 and E_2 are elastic moduli describing the tissue, η is a viscoelasticity coefficient, and ε is the strain. Defining $\varepsilon(t) = \delta r_0/\bar{r}_o$ and $\sigma(t) = f_{oi}\delta p_i - f_{oo}\delta p_0$ from the thick wall cylinder model and combining (6), (9), and (11), a constitutive relation between arterial variation and inner and outer pressure under the PVDF ring can be obtained accounting for viscoelasticity,

$$\frac{d\varepsilon}{dt} = \frac{\frac{E_1}{\eta}\left(\frac{\eta}{E_2}\left(f_{oi}\frac{dp_i}{dt} - f_{oo}\frac{dp_o}{dt}\right) + \left(f_{oi}\delta p_i - f_{oo}\delta p_o\right) - E_1\varepsilon\right)}{E_1 + E_2} \tag{12}$$

Changes of inner pressure also be related to other variables by an alternative arrangement of (12), i.e.

$$\frac{dp_i}{dt} = \frac{E_2}{\eta}\frac{\left(f_{oi}\frac{\eta}{E_2}\frac{dp_i}{dt} + \delta p_0\right) + \left(\frac{\eta(E_1+E_2)}{E_2}\frac{1}{r_o}\frac{dr_o}{dt}\right) + E_1\frac{\delta r_o}{r_o}}{f_{oi}} \tag{13}$$

3.5 Model Summary

To summarize the sensor model, two independent equations are present: a static relationship relating perturbations in pressure on the sensor to arterial radius (δp_o vs δr_o), in (9) and a dynamic equation for either artery radius or internal pressure (12) or (13) incorporating basic viscoelastic behavior, with variables δp_i, δp_o, and δr_o. Once δp_o can be measured, as with the PVDF sensor, this is sufficient to solve for the other two variables, with δr_i also available via (6) and (7).

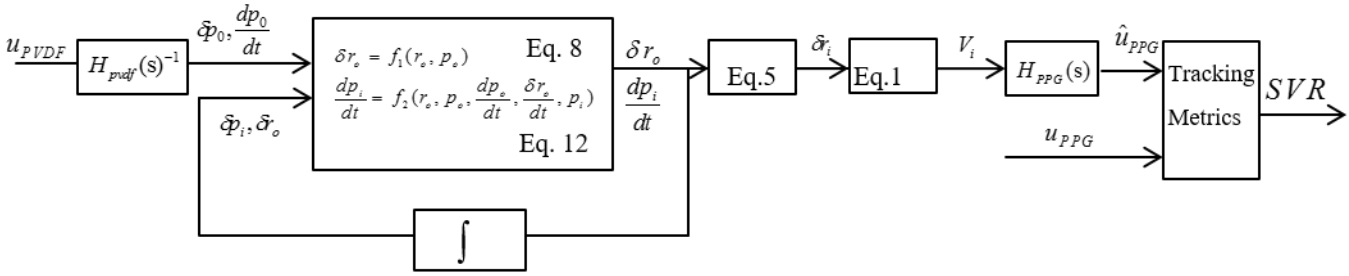

Fig. 7 During implementation, piezoelectric sensor voltage, u_{PVDF}, is used to infer changes in external pressure, p_o, which is used to calculate perturbations in internal artery pressure, p_i, and radii, r_i and r_o via the model from Section 3.4. These estimates are used to predict what changes in internal artery volume, V_i, would be at the nominal artery radius, along with an anticipated PPG sensor output, $\hat{u}_{PPG}$. Comparison to the actual PPG sensor output, u_{PPG} is done to estimate systemic vascular resistance, SVR, by metrics described in Section 4.2.

However, all of the above relationships are dependent on the average arterial radii during the cardiac cycle ($\bar{r}_i$ and $\bar{r}_o$) which in reality will vary over many cycles as vascular resistance changes. Thus, the model is used in inverted fashion for nominal, assumed constant, arterial radii, as shown schematically in Fig. 7. Then, an input-output relationship between PVDF and PPG measurements can be established for parameter identification and peripheral vascular resistance/SVR estimation. Short term fluctuations in pressure on the PVDF band, inferred from piezoelectric sensor output voltage, are used as an input to the nonlinear state-space models (13) for differential arterial pressure. Pressure is then related to inner and outer arterial radii via (6) and (9), with inner radius used to predict blood volume under PPG sensor, which can be compared to the measured PPG response, $\hat{u}_{PPG}$. Discrepancies between predicted and measured PPG response are then attributed to changes in arterial radius, as described in the following section.

It should be emphasized that much more detailed arterial tissue modeling has been done in previous works on artery and tissue mechanics. Tissue modeling in this work draws only the most apparent features in observed data, and even then associates behavior such as compressibility and hysteresis only with individual model elements, when in reality the tissue structure under the sensor band is quite heterogeneous. In the following sections, model validation is performed by comparing invasive measurements of SVR to that implied by changes in estimated arterial radius using this model, assuming peripheral vascular resistance and SVR to change effectively proportionally.

3.6 Model Parameters

In the sensor and artery model from Section 3.5, exact parameters related to arterial radius and tissue properties are not directly available unless related solely to the PVDF sensor. Instead, representative values from the literature were selected as approximate values, as listed in Table I. In addition, the gain of the pulse plethysmograph was observed to vary substantially from subject to subject, and thus was estimated individually by optimizing the fit between the measured PPG signal and a predicted PPG signal generated from the PVDF sensor measurement at the onset of testing. The first ten cardiac cycles during swine experiments were used to calibrate the PPG gain in each of experiment.

Table 3 Model parameters

Variable	Parameter	Value	Units
Nominal values used throughout testing:			
$\bar{r_o}$	Nominal artery radius	1.5	mm
$\bar{R}$	limb radius	50	mm
E_s	sensor modulus	2.5	GPa
t	PVDF thickness	52	μm
T	ring tension	2	N
d_{31}	piezoelectric coefficient	11×10^{-12}	C/N
γ	ring compliance	1.5	mm^3/Pa
Identified from first 10 cardiac cycles for first swine subject, used in all further testing:			
E_1	viscoelastic modulus 1	200	kPa
E_2	viscoelastic modulus 2	1	kPa
η	viscoelastic damping ratio	1000	
Adjusted for each swine using first 10 cardiac cycles:			
K_{PPG}	PPG gain	2000~5000	

3.7 SVR Tracking Metrics

As discussed above, neither PPG nor piezoelectric sensing mechanisms provide absolute measurement of arterial radius or pressure, but rather time-varying perturbations from those signals' average values. However, the sensors' relative amplitudes and dynamic responses (i.e., relative hysteresis) remain dependent on artery radius changes. Fig. 8 plots modeled PPG vs. PVDF sensor output over a single cardiac cycle for two values of mean arterial radius; experimental measurements for cycles with an approximately equivalent SVR change (as measured invasively) are also shown. First, the model for local tissue and sensor behavior beneath the piezoelectric ring shows acceptable agreement with experimental data, though there is clearly more complexity in the true physiology than in the proposed model.

Second, it is clear that both in the model and experimental behavior, PPG output increases to a proportionally greater degree than PVDF output when mean arterial radius increases and SVR decreases. This provides one method by which changes in arterial radius may be inferred from relative change in PPG and piezoelectric sensor signals.

Third, a key observation during swine testing is that the relative amplitude of hysteresis observed during arterial expansion and contraction correlates very strongly with SVR, which is also observed in Fig. 8: for larger artery radius, the degree of hysteresis changes relative to the total amplitude of the signal.

Based on the observations above, two metrics for estimating changes in peripheral vascular resistance/SVR are proposed. Figure 9 shows a series of hysteresis loops formed by plotting PPG sensor output versus PVDF sensor output at series of cardiac cycles occurring over a two-hour period. The pulse transit time delay is constant due to the different location of two sensors and had been adjusted base on the peak time of two signals. Solid loops indicate experimentally obtained data, with SVR know to be changing and presumed to be accompanied by arterial radius changes. Dashed loops are generated using measured piezoelectric sensor data to predict PPG response if

arterial radius were constant, using the model from Section III. Mismatch between the predicted and observed sensor behavior is taken to be indicative of changes in arterial radius.

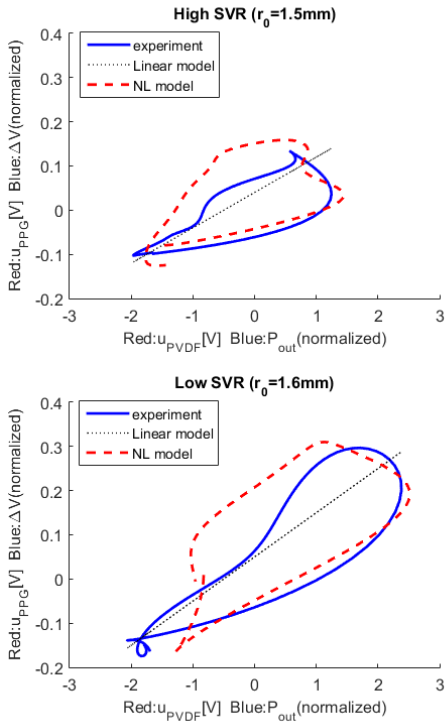

Fig. 8 Hysteretic response visible between differential pressure and volume during arterial expansion and contraction.

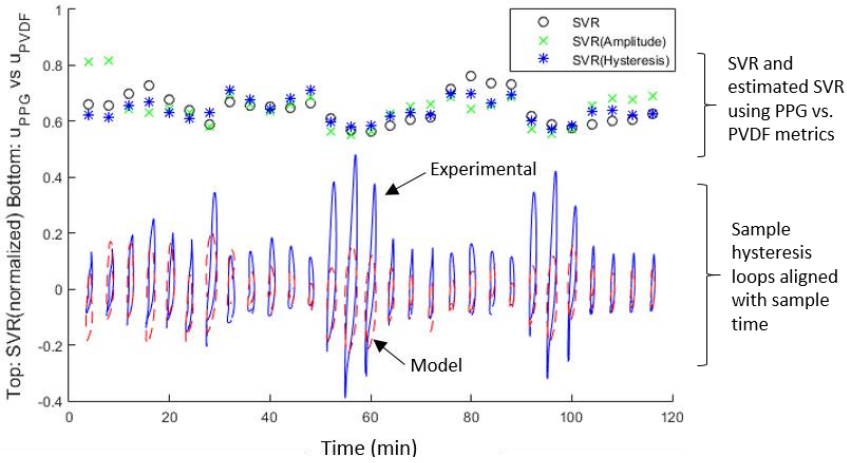

Fig. 9 Examples of hysteresis behavior and SVR tracking over a two-hour experiment, with individual cardiac cycles shown below to demonstrate changes in amplitude and hysteresis behavior, aligned with times at which sample hysteresis loops were collected.

Two metrics are proposed for quantifying the differences between simulation and experimental behavior in order to predict SVR in the current work. In both cases, during each cardiac cycle an ellipse is generated to fit the hysteresis loop between the PPG and piezoelectric sensor outputs for both the experimental and projected (hypothetical fixed radius) response. The long chord of the ellipse is used to approximately represent the amplitude of volume change and the ratio of short chord to long chord to represent hysteresis. The estimated SVR metric is obtained by linear regression of invasive SVR measurement and relative amplitude or hysteresis from first 10 cardiac cycle. The intercept of the two formula are proportionally changed with different PPG gain, which also individually calibrated with first ten blood cycles data.

The first metric for estimated SVR ($\widehat{SVR}$) is based on relative amplitude, and is formulated

$$\widehat{SVR_1} = 0.02(L_s - L_e) + 0.52 \tag{13}$$

with *L* being the long chord of an ellipse fit, where subscript *s* indicates the simulated PPG output given the current PVDF output and subscript *e* indicates the actual experimental output. Effectively, this metric is selected to capture the mismatch increased signal amplitude when arterial radius changes from baseline, while the ratio of PPG amplitude to PVDF amplitude remains approximately constant if only blood pressure changes at a fixed nominal arterial radius.

Similarly, when SVR increases, observed experimental hysteresis will be larger than projected based on the model with constant nominal radius. This is quantified as

$$\widehat{SVR}_2 = -0.166(h_s - h_e) + 0.7 \tag{14}$$

where *h* is a hysteresis measurement obtained from

$$h_{s,e} = \frac{L_{s,e} - S_{s,e}}{L_{s,e}} \tag{15}$$

where *S* is the short chord of the ellipse fit to the hysteresis loop.

Constant coefficients in (13) and (14) are selected to scale estimated SVR to normalized 0 to 1 scale for comparison to changes in the invasively measured SVR. Normalization was done using the first 10 cardiac cycles in each experiment, also removing residual drift from numerical integrations if necessary. In most practical applications, baseline SVR would not be known, providing estimates of relative change in SVR from initial baseline would be the key outcome of SVR tracking. Examples of changes in SVR and metric outputs are shown at the top of Fig. 9 for the sample cardiac cycles shown.

3.8 SVR Tracking Performance

Proposed metrics for SVR tracking were tested on three swine experimental subjects. SVR was tracked invasively using carotid artery catheterization. Cardiac output and central venous pressure were measured using a Swans Ganz catheter having continuous thermodilution capabilities. The combination of data was used to compute the SVR values. The PVDF sensor and PPG sensor were placed adjacent to one another on same swine appendage (forearm). All the signals were collected and stored using a Biopac MP150 device and analyzed retrospectively. Norepinephrine (a powerful arterial vasoconstrictor agent) was infused into the blood to periodically increase SVR during each test, and SVR dropped when each infusion stopped.

SVR estimates obtained by the proposed SVR tracking metrics, using amplitude and hysteresis, respectively, of simulated versus observed PPG to PVDF signal relationship, are shown in Fig. 10. SVR tracking was most accurate with the first subject, Fig. 10, which showed generally close agreement between both amplitude- and hysteresis-based SVR estimates and invasive SVR measurements after an initial time period required for parameter identification to converge. Greater discrepancies are observed in the second and third tests, but both methods generally capture increases and decreases in SVR. In all three experiments, estimates based on hysteresis variation performed better than estimation based on relative PPG to PVDF amplitude. Worst tracking was observed at the conclusion of experiments with Swine 1 and Swine 2, which may have indicated further physiological changes accumulating during the testing period.

For comparison to existing non-invasive SVR estimation, SVR was also estimated using PPG waveform analysis by the method proposed by A. Scholze et al [16]. The basic idea of PPG waveform analysis is that the ratio of first and second peaks of each cardiac cycle proportional related with vascular tone. Those peaks were chose when the first order derivative of PPG signal cross zero. SVR estimation based on PPG waveform alone was much less consistent than for metrics combining PPG and piezoelectric sensor information. For example, PPG-only estimates showed good agreement with invasive SVR in test 1, but very poor tracking of SVR in test 3.

Estimator performance was evaluated based on the mean and maximum absolute percentage errors of SVR tracking, as defined by

$$\frac{1}{N}\sum_{n=1}^{N}\frac{|\widehat{SVR}-\overline{SVR}|}{\overline{SVR}} \tag{16}$$

and

$$\max_{n}\frac{|\widehat{SVR}-\overline{SVR}|}{\overline{SVR}} \tag{17}$$

respectively, where N is the number of cardiac cycles and $\overline{SVR}$ is the invasively measurement value for SVR in each cycle.

Performance of non-invasive SVR estimation from combined PPG and piezoelectric sensing, as well as PPG waveform analysis alone is summarized in Table II. As can be seen, in all three cases the proposed SVR estimator performance was superior to that based on PPG waveform analysis, most dramatically with respect to the worst case estimates (maximum absolute percentage errors) obtained by each method.

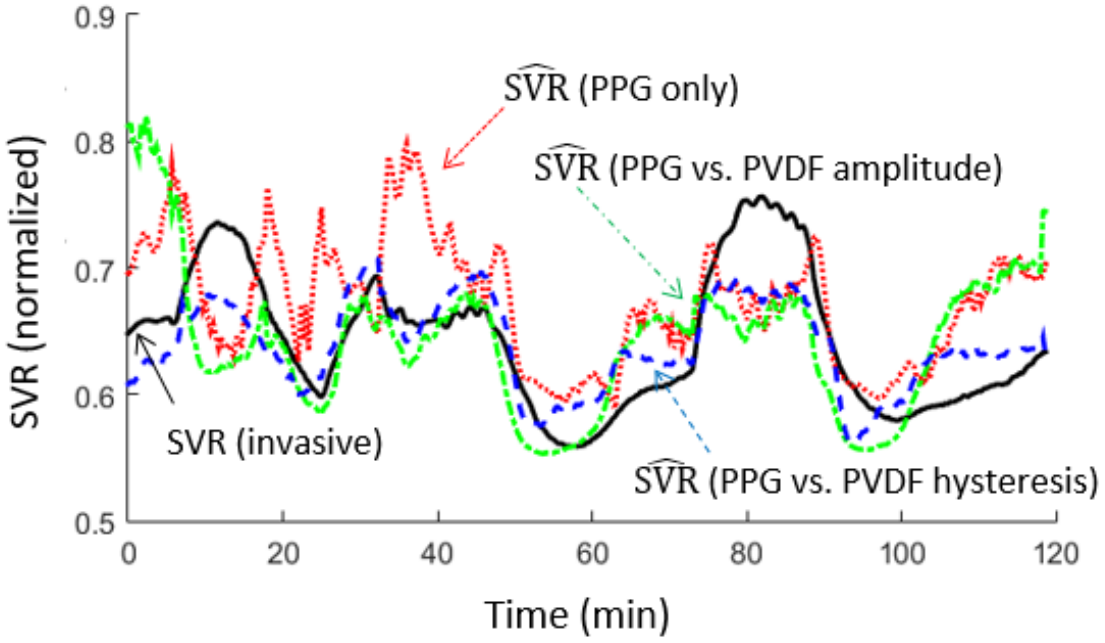

Fig. 8 SVR tracking results for swine test 1

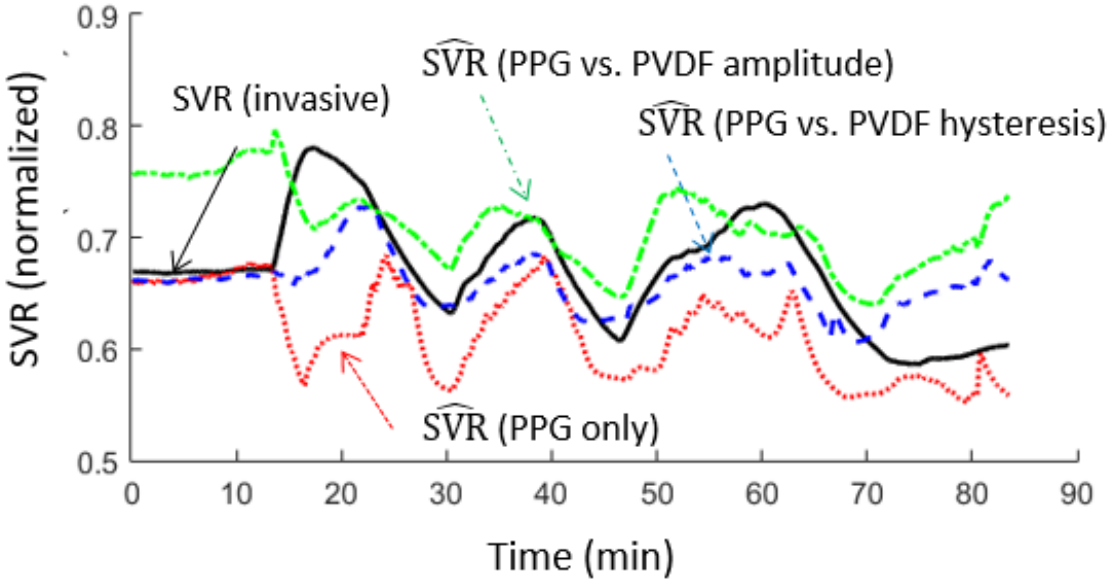

Fig. 9 SVR tracking results for swine test 2

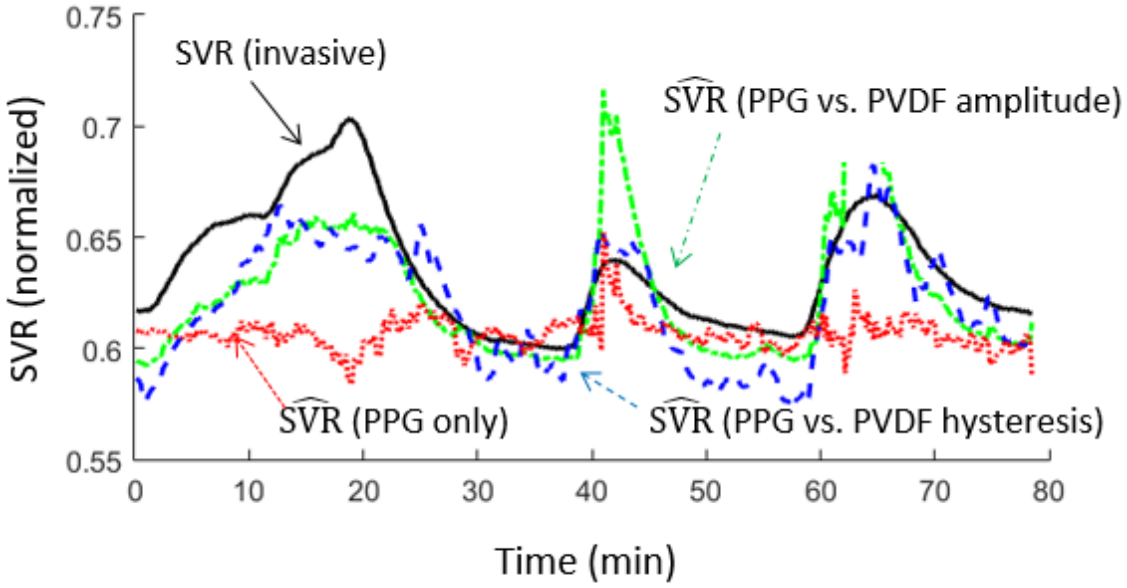

Fig. 10 SVR tracking results for swine test 3

Performance of non-invasive SVR estimation from combined PPG and piezoelectric sensing, as well as PPG waveform analysis alone is summarized in Table 4. As can be seen, in all three cases

the proposed SVR estimator performance was superior to that based on PPG waveform analysis, most dramatically with respect to the worst case estimates (maximum absolute percentage errors) obtained by each method.

Table 4 SVR estimation performance for different methods: By hysteresis = estimated based on variation in PPG vs. PVDF hysteresis; By relative amplitude = estimated based on change in relative PPG vs. PVDF amplitude; By PPG wave alone = estimated based on features of PPG waveform.

Test	Mean absolute percentage error			Maximum percentage error			Root mean square error (RMSE)		
	By hyst-eresis	By relative amplitude	By PPG wave alone	By hyst-eresis	By relative amplitude	By PPG wave alone	By hyst-eresis	By relative amplitude	By PPG wave alone
1	4.7%	8.7%	10.2%	14%	29%	50%	0.036	0.072	0.074
2	3.7%	8.0%	9.6%	17%	27%	41%	0.037	0.073	0.093
3	4.5%	5.6%	12.4%	15%	19%	77%	0.037	0.047	0.112

A Bland-Altman plot of estimation results for swine test 2 is shown in Fig. 13. It shows that the estimates based on hysteresis variation performed better than other two methods in absolute systematic error and proportional error.

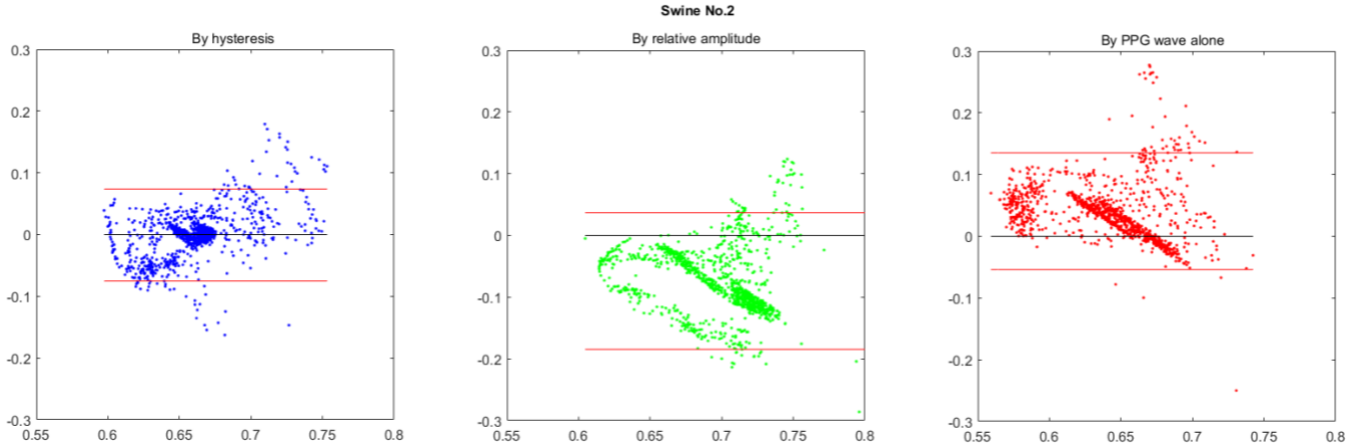

Fig. 11 Bland-Altman plot of SVR tracking results for swine test 2

Chapter 4 Estimation of Peripheral Artery Radius via Kalman Filtering

In this chapter, we proposed a method for estimating peripheral arterial radius based on the extended Kalman filter and the local nonlinear artery model in chapter 3. The current work focuses on use of the PPG and PVDF sensors to form a type of input-output relationship across a simple dynamic model for local deformation of the artery and other tissue. Arterial radius is introduced as an augmented state in an extended Kalman filter, with the Kalman filter then used to perform system identification and tracking of relative changes in arterial radius over time on a swine subject[40].

4.1. State Space Model and Estimator Design

To track arterial radius, the pair of sensors is treated as acting in a fictitious input-output relationship, i.e., an "input" exterior pressure (known by the PVDF sensor) is treated as generating differential changes in volume at the PPG sensor via the intervening local tissue dynamics. In reality, pressure fluctuations are being driven by the interior pressure in the artery, and techniques such as a disturbance observer might also be effective, but the input-output formulation is well-suited to parameter tracking by system identification methods.

For continuous arterial radius tracking, the simple local arterial dynamic model in (13) is augmented by the radii to be monitored. Let the state variables, x_i, and the inputs for the system, u_i, be defined as follows:

$$\begin{bmatrix} x_1(t) \\ x_2(t) \\ x_3(t) \end{bmatrix} = \begin{bmatrix} r_o(t) \\ \delta p_i(t) \\ r_i(t) \end{bmatrix}, \quad \begin{bmatrix} u_1(t) \\ u_2(t) \end{bmatrix} = \begin{bmatrix} \delta p_o(t) \\ \dfrac{dp_o(t)}{dt} \end{bmatrix} \tag{18}$$

The inputs to the system are thus quantities that can be extracted directly from PVDF sensor output, provided properties of the PVDF ring and piezoelectric sensing circuit are well known, and states are a combination of the original dynamic model for the system and parameters for system identification.

Then, the discretized nonlinear artery state model and output model can be described by

$$\mathbf{x}_k = f\left(\mathbf{x}_{k-1}, u_{k-1}\right) + w_k \tag{19}$$

$$z_k = h\left(\mathbf{x}_k\right) + v_k \tag{20}$$

Where w_k and v_k are process noise and measurement noise, which are assumed to be independent, zero mean white Gaussian noise with covariances Q_k and R_k respectively. In this model $f(x_{k-1}, u_{k-1})$ is the nonlinear part of the state model, which from (8)-(13) also can be described as:

$$f(x_{k-1}, u_k) = \begin{bmatrix} \sqrt{\dfrac{\pi\left(\bar{R} + \dfrac{2\bar{R}^2}{E_s t} u_1\right)^2 - V_o + \gamma u_{1_k}}{2\pi}} - x_{1_{k-1}} \\ \dfrac{E_2}{\eta} \dfrac{\left(f_{oo} \dfrac{\eta}{E_2} u_{2_k} + u_{1_k}\right) + \left(\dfrac{\eta(E_1 + E_2)}{E_2} \dfrac{x_{1_k}}{x_{1_{k-1}}}\right) + E_1 \dfrac{x_{1_k}}{x_{1_{k-1}}}}{f_{oi}} \\ \dfrac{1}{E}(f_{ii} x_{2_{k-1}} - f_{io} u_{1_k}) x_{3_{k-1}} \end{bmatrix} \tag{21}$$

A nonlinear output model, $h(\mathbf{x}_k)$, from (5), can then be written as:

$$h(x_k) = K_{PPG} h_{PPG} \pi L_{PPG} ({x_{3_k}}^2 - {x_{3_{k-1}}}^2) \tag{22}$$

The extended Kalman filter linearizes the nonlinear-state model for each new estimate as it becomes available. From the above dynamic model the inside radius of artery can be estimated by the following extended Kalman filter algorithm.

1) Prediction of State:

$$\hat{\mathbf{x}}_k = f\left(\hat{\mathbf{x}}_{k-1}, u_{k-1}\right) + w_k \tag{23}$$

2) Estimation of Error Covariance Matrix:

$$P_{k|k-1} = F_{k-1} P_{k-1|k-1} F_{k-1}^T + Q_k \tag{24}$$

Where

$$F_{k-1} = \left.\frac{\partial f}{\partial x}\right|_{\hat{x}_{k-1|k-1}, u_k} = \begin{bmatrix} -1 & 0 & 0 \\ -\dfrac{E_2}{\eta} \dfrac{\left(\dfrac{\eta(E_1 + E_2)}{E_2} + E_1\right) \dfrac{1}{x^2_{1_{k-1}}}}{f_{oi}} & 0 & 0 \\ 0 & \dfrac{f_{ii}}{E} x_{3_{k-1}} & -\dfrac{f_{io} u_1}{E} \end{bmatrix} \tag{25}$$

3) Computation of Kalman filter gain

$$K_k = P_{k|k-1} H_k^T (H_k P_{k|k-1} H_k^T + R_k)^{-1} \tag{26}$$

where

$$H_k = \left.\frac{\partial h}{\partial x}\right|_{\hat{x}_{k|k-1}} = \begin{bmatrix} 0 & 0 & 2K_{PPG}h_{PPG}\pi L_{PPG}x_{3_{k|k-1}} \end{bmatrix} \tag{25}$$

4) Update of the Error Covariance Matrix:

$$P_{k|k} = (I - K_k H_k)P_{k|k-1} \tag{27}$$

5) State Estimation:

$$\begin{aligned} \hat{\mathbf{x}}_{k|k} &= \hat{\mathbf{x}}_{k|k-1} + K_k\left[z_k - h(\hat{\mathbf{x}}_{k|k-1})\right] \\ \rho &= \frac{8L\eta}{(\pi\hat{r}_i^4)} \end{aligned} \tag{28}$$

The estimator's predicted output, $h(\hat{\mathbf{x}}_{k|k-1})$,can also be considered a prediction of the PPG output, and is also referred to as $\hat{U}_{PPG}$.

4.2. Experimental Setup and Signal Preparation

Arterial radius estimation was implemented of test data acquired from a swine test subject. The PVDF sensor and PPG sensor were placed adjacent to one another on the same swine foreleg. All signals were collected and stored using a Biopac MP150 device and analyzed retrospectively.

For validation, arterial radius estimates are compared to invasively-measured SVR, tracked using carotid artery catheterization. It is important to note that while peripheral vascular tone is often considered the dominant factor in determining SVR, anticipated to be approximately proportional to ri-4 should arterial response be relatively uniform throughout the periphery, SVR and arterial radius may potentially diverge under certain cardiovascular scenarios. SVR was computed from Cardiac output and central venous pressure were measured using a Swans Ganz catheter and used to compute the SVR values. Changes in SVR were induced by periodic infusion of norepinephrine, with SVR increasing during infusion and decreasing when each infusion stopped.

Prior to Kalman filter implementation, PVDF and PPG sensor data were conditioned to remove certain known artifacts. PVDF sensor output was passed through a band-pass filter to remove long term drift and reduce high frequency noise. The PPG waveform was subject to sudden amplitude changes due to an automatic gain controller which adjusts the gain of the amplifier automatically based on the amplitude of the input signal; this auto-gain could not be disabled with

the existing software. In this study, when the artery suddenly contracted, it was found that when if amplitude of PPG signal dropped to half of its original amplitude, the controller doubled the gain. This automatic gain control occurred in the swine test at about 65 minutes. Therefore, we let the gain of PPG sensor, K_{PPG}, be multiplied by two when the amplitude of the voltage signals in one blood cycle dropped to less than 0.1V.

Parameters not identified by the Kalman filter, such as the viscoelastic moduli, E_1 and E_2 and viscoelastic damping coefficient, η, were tuned to minimize error between the actual and predicted PPG output over the first ten cardiac cycles, while arterial radius was assumed to be constant. The initial arterial inner radius was arbitrarily set as 1.5 mm, based on typical swine artery dimensions.

4.3. SVR and blood pressure estimation

To assess accuracy of arterial radius estimation, the estimated artery radius is converted to a vascular resistance by

$$\rho = \frac{8L\eta}{(\pi \hat{r}_i^4)} \tag{29}$$

where ρ is the estimated local resistance to blood flow, L is the length of the vessel, and η is viscosity of blood which was taken to be $3.5\times10^{-3} Pa\cdot s$. We compared the simulated vascular resistance to invasive SVR measurement,

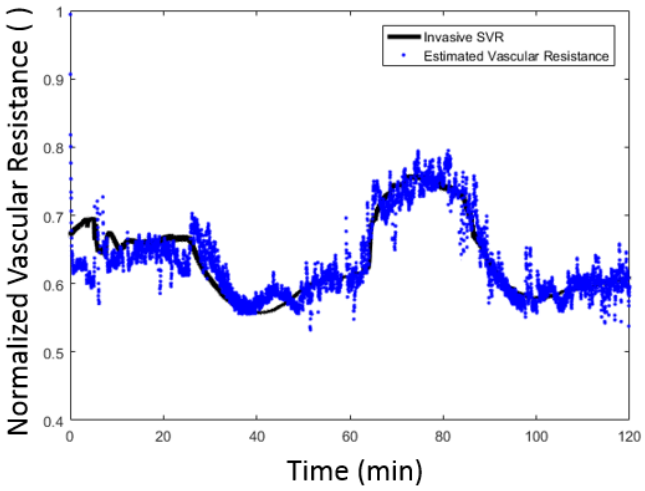

Fig. 12 Estimated vascular resistance at the PVDF and PPG sensor location closely tracks changes invasive systemic vascular resistance measurements in proof of concept testing on a swine test subject.

normalizing by the real and estimated resistance in the first 10 cardiac cycles. Vascular resistance tracking is shown in Fig. 14. As can be seen, the local vascular resistance estimate closely track SVR through the majority of the testing period. Large fluctuations in SVR in the test subject are caused by starting and stopping infusions of norepinephrine. The resulting major trends in SVR are best matched by the estimated changes in arterial radius. On the other hand, there are indications of additional dynamics present, as in oscillations in predicted radius at very low SVR, and the estimated radius is very sensitive to noise.

As an additional validation given data available from swine testing, Figs. 15(a) and 15(b) show estimated systolic and diastolic pressure estimates, respectively, in comparison to invasive arterial blood pressure measurements. It should be emphasized that the PVDF sensor is not intended to serve as an absolute pressure measurement system, due to inherent drift of the piezoelectric sensing mechanism in absence of an additional reference. In addition, there are substantial additional un-modeled fluid dynamics between arterial and PVDF sensor locations. Nonetheless, use of model-based state estimation does permit the sensor to capture some major trends in blood pressure fluctuation, which provides some additional confidence in the proposed approach for tracking vascular behavior. On the other hand, blood pressure estimation is subject to much more substantial non-physical spikes in the state estimates, which is indicative of greater sensitivity of

the blood pressure terms in the system model to noise and numerical error, and also reflects the fact that PPG output reflects filter states that are directly tied to volume but only indirectly to pressure.

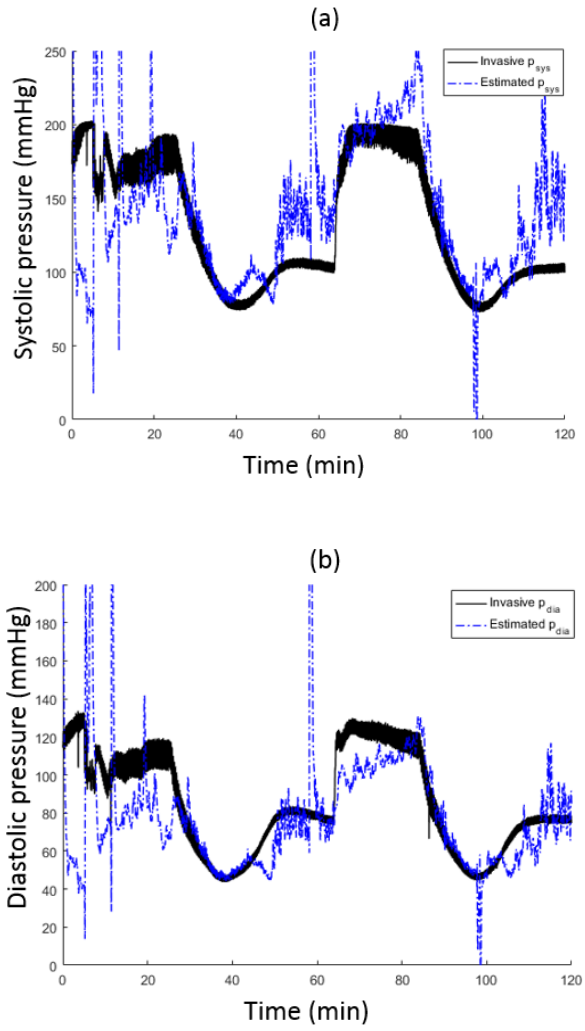

Fig. 13 Even though no pressure reference is present, estimated blood pressure within the PVDF ring roughly tracks blood pressure measured by an arterial line, though with substantially greater errors than volume estimation for vascular resistance.

Major limitations of this work include the scope of validation – a single swine subject at present – as well as need to calibrate several parameters of the model before radius tracking can be performed, such as parameters describing viscoelastic arterial dynamics. Nonetheless, as a proof-

of-concept test, vascular resistance tracking results show promise for a simple, non-invasive means for tracking changes of vascular resistance at a variety of care settings.

4.4. Validation of Artery Radius Estimation with Ultrasound Videos

As a further attempt to validate arterial radius estimation, a method was developed to calculate the area based on imaging processing of ultrasound videos, as the videos are made by a sequence of pictures. The ultrasound probe was place near the PVDF/PPG sensor, and both units were placed on a swine's foreleg during procedures to manipulate vascular resistance.

The ultrasound image is formed by millions of pixels, each pixel representing a point in an image. For the ultrasound system used in this experiment, each pixel is formed by three different components extracted from the ultrasound signal, which are represented light in three colours: red, green and blue, at different intensities. As direct ultrasound signal was not available from the commercial system, image processing had to be performed using the colorized output video. As a result, each single frame was represented by three matrices (one for each color) that included the information on the intensity of each component at every pixel. Knowing this, we were able to represent each matrix as a surface on a three-dimensional space. By analysing changes in colour intensity, changes in the artery's area are determined.

However, not every pixel that is displayed on these videos was subject to study, we focused on the area where the radial artery is locaded (inside the red rectangle in Fig. 16). Because the artery occupies only small portion of the field-of-view of a conventional ultrasound monitor when imaged at the swine foreleg, several processing steps had to be performed to measure motion of the artery walls.

Fig. 14 Sample ultrasound video with artery highlighted

For each frame, the image was processed by the following steps:

a) Obtain the pixel intensity information of the space where the artery is located shown in Fig. 17.

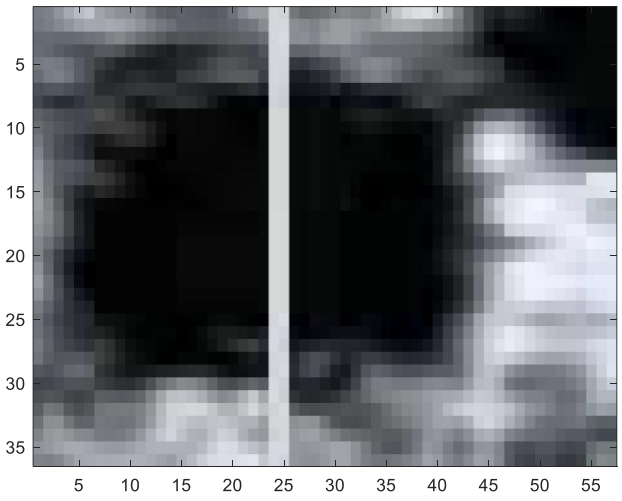

Fig. 15 Selected ultrasound image near artery is located

b) Eliminate from the matrix the data that is on the right of the centre of the artery. This is done using coordinates calculated at the beginning of the analysis.

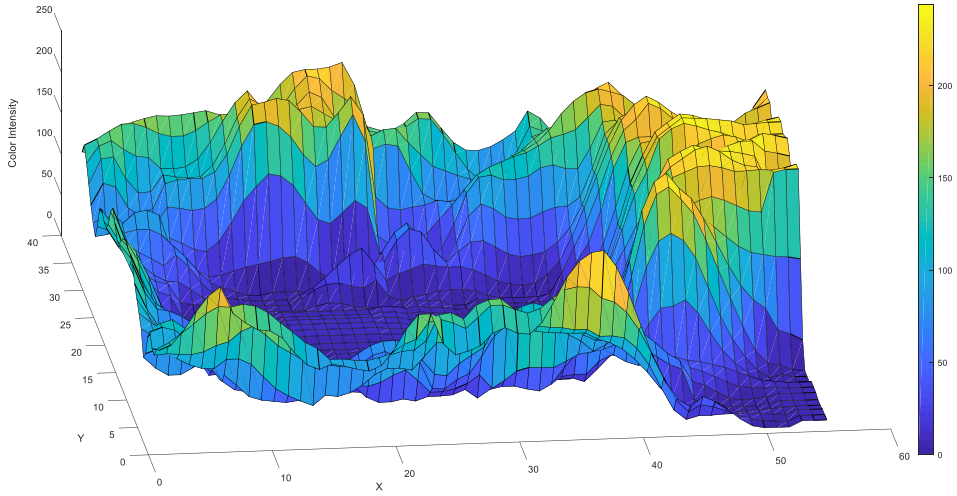

Fig. 16 3D representation of pixel intensity

c) Create the 3D contour of artery, shown in Fig.18. This is created by the Matlab function 'contour(x, y, Z)', where Z contains light density values on the x-y plane. In order to get a closed curve when calculating the contours, as some of them may not close, the data from the matrix is enclosed in a larger field of view one with dimension (n+2, n+2) that surrounds the artery with values higher than any pixels present in the frame.

d) Calculate multiple contour boundaries at varying intensity levels. This was done as it is difficult to determine what the exact boundary of the artery is from the video, and averaging of multiple candidate boundaries was expected to provide more accurate measurement. These contours are calculated as the intersection between the surface generated with the colour intensity data and equidistant planes perpendicular to the Z axis. The distance chosen between the planes was 10 (intensity of color). When analysing the final results this will be useful to determine which contour represents the real boundary of the artery.

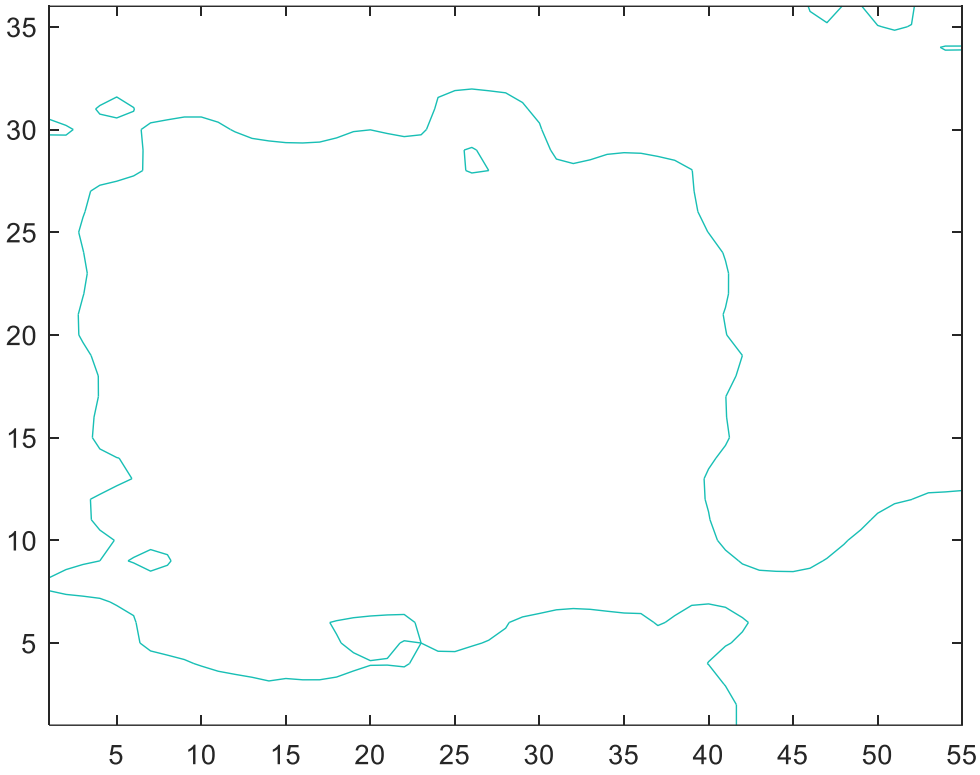

Fig. 17 Contour representing the boundary of the artery

e) Calculate arterial area, based on coordinates of the points in the contour, the area can be now calculated. The area is calculated using the 2-D polygon area equation:

$$A = 0.5 \sum_{i=0}^{n-1} (x_i y_{i+1} - x_{i+1} y_i) \quad (30)$$

where the vertices of the polygon under consideration are taken to be $(x_0, y_0), (x_1, y_2), \ldots, (x_n, y_n)$ in order.

f) Once contours are calculated for all frames, filter time-domain information. A band pass filter was used to keep the information from the dominant frequency of motion (heartrate) and its first four harmonic frequencies; all other frequencies are attenuated. The band pass frequency was found by Fourier analysis of all the swine videos. The formulas used to design this filter were:

$$F_0 = \sqrt{F_H * F_L} \quad (31)$$

$$\omega_0 = 2\pi F_0 \tag{32}$$

$$Q_0 = \frac{F_0}{F_H - F_L} \tag{33}$$

$$G(s) = \frac{\frac{\omega_0}{Q_0} * s}{s^2 + \frac{\omega_0}{Q_0} * s + \omega_0^2} \tag{34}$$

Where $F_H = 10Hz, F_L = 0.01Hz$

After all the processing steps, the radius of the artery can be finally analysed from the image. The final result of the area calculation from one sample videos is shown in Fig. 20.

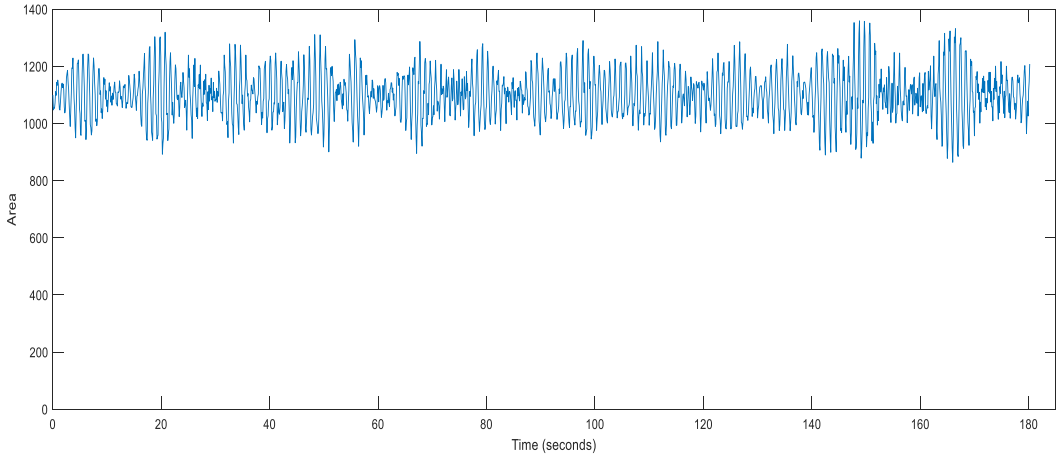

Fig. 18 Estimated artery area from a sample ultrasound videos. The image processing algorisms can capture artery changes from both the cardiac cycle and the respiratory cycle. Here, the area is represented by the number of pixels.

It can be clearly seen from the result that changes in the area are small during each cardiac cycle, which is averaging 8%. These changes are generated by each heartbeat which increases pressure when pumping blood through the arteries. For each video, we

calculate the mean artery area by averaging the area number for each cardiac cycle and also the average of artery area changes in each cycle for later comparisons.

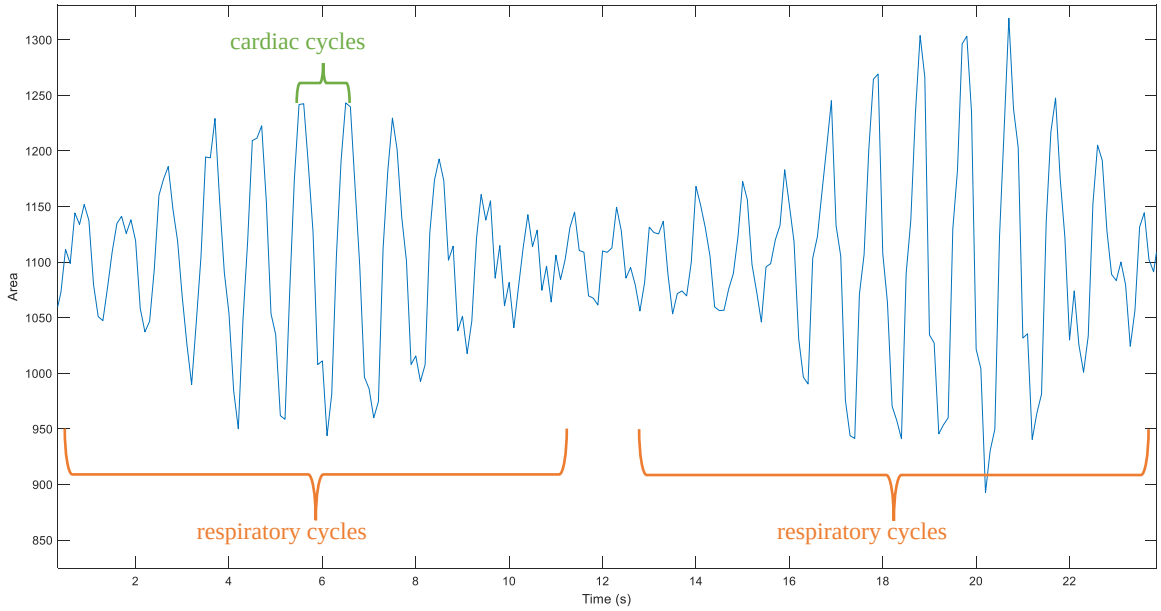

Fig. 19 Details of artery area changes during the cardiac and respiratory cycles from a sample ultrasound videos.

The beat-to-beat amplitude of the area changes is not constant over time. This is caused primarily by the breathing of the swine, or respiratory cycle, but also by changes in mean arterial radius due to vascular resistance changes. Respiratory effects arise because the left side of the heart behaves differently at different points in the respiratory cycle. During inspiration, expansion of the lungs and pulmonary tissues causes pulmonary blood volume to increase, which transiently decreases the flow of blood from the lungs to the left atrium. Therefore, left ventricular filling decreases during inspiration. In contrast, during expiration, lung deflation causes flow to increase from the lungs to the left atrium, which increases left ventricular filling. The net effect of increased rate and depth of respiration, however, is an increase in left ventricular stroke volume and cardiac output.

To validate the effectiveness of the estimation method proposed, different videos were evaluated on a swine subject. Ten different videos were chosen, these videos were chosen using the information of the systolic pressure of the swine obtained during the experiment in moments when significant changes in the area were expected, as increases in systolic pressure will increase the area of the artery.

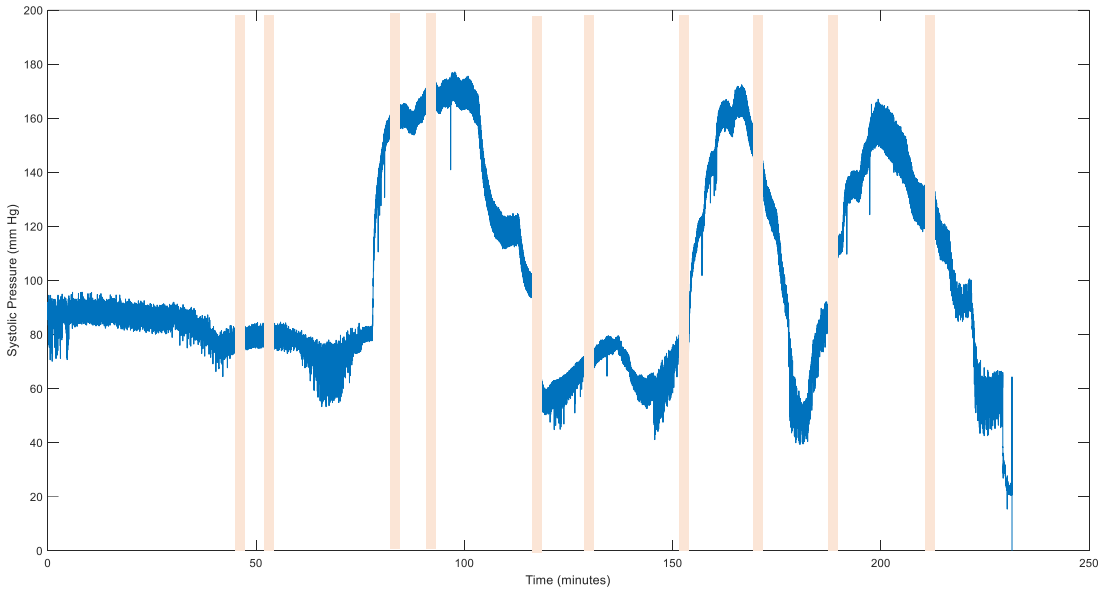

Fig. 20 Systolic blood pressure (blue line) during experiment and ultrasound video intervals(orange area) studied

Arterial radius is estimated as an augmented state with the same extended Kalman filtering method in the previous sectoins. Then, the area of the artery can be calculated as:

$$\hat{\mathrm{A}} = \pi \hat{r}_i^{\,2} \tag{35}$$

The mean average of the estimated artery area is compared with the measurement from ultrasound videos, at the same time periods, as shown as Fig.25. As can be seen, the estimation results shown a reasonable agreement with ultrasound measurements. However, the absolute value is not always perfectly matched between the two method. We believe that the ultrasound imaging is likely the less accurate measurement in those time periods, which corresponded to some of the smallest arterial radii. This resulted in the worst quality videos of the small artery area, limiting the accuracy of results from the ultrasound. It is also possible that some assumptions from the wearable sensor estimation model lose validity at smaller arterial radii,

though vascular resistance tracking generally continued to follow invasive measurement during these time periods.

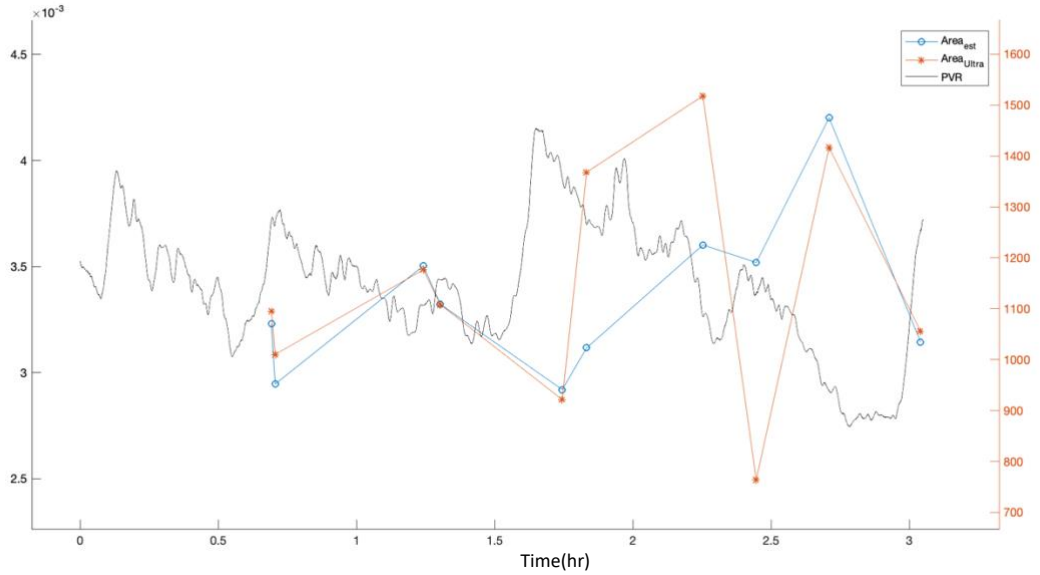

Fig. 21 Comparison of estimation of artery area (blue line) with EKF and estimated area by ultrasound videos (orange line). Normalized PVR (black line) is estimated by artery radius, which is inversely related to the area of the artery and available on a continuous basis

The beat-to-beat area oscillations (i.e., expansion and contraction of the artery during a single pulse) were also be compared with the data obtained from the non-invasive sensor that was tested at the same time. To calculate these oscillations the amplitude from dominant frequency (the one corresponding with the heartbeat ~ 1 Hz) from the Fourier analysis was used.

As it can be seen, the measurements follow the same trend most of the cases, though ultrasound data is even noisier over these timeframes. From the data obtained it appears that an increase in pressure results in a smaller amplitude change in the artery cross-sectional area. This phenomenon can be explained as the result of the arteries' smooth muscle cells contracting being the primary cause of blood pressure increases in these experiments (stimulated by infusion of norepinephrine). This reduces the effect of beat-to-beat pressure fluctuations on the artery area. In other words, the

changes in arterial radii generated by heartbeats are not as significant when blood pressure has increased due to vasoconstriction.

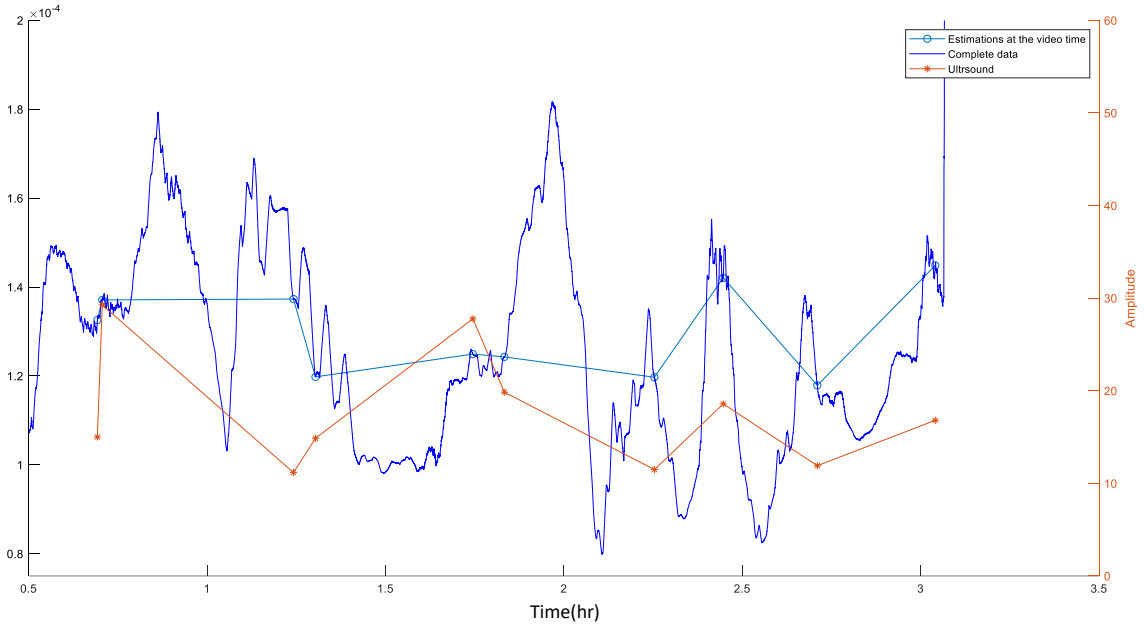

Fig. 22 Comparison of changes of artery area (blue line) in each cardiac cycle with EKF and estimated area changes by ultrasound videos (orange line).

4.5. Conclusion

A model and estimator based on the extended Kalman filter are proposed for tracking radius of peripheral arteries, making use of a simple mechanical model of arterial and tissue dynamics to account for varying response of a pulse plethysmograph and a piezoelectric pressure sensor. In proof-of-concept testing on a swine test subject, local vascular resistance calculated from arterial radius estimates at the ring location show good agreement with overall systemic vascular resistance, while capturing more roughly other features of local cardiovascular behavior. A simple image processing algorism is introduced to measure the area of small artery with ultrasound videos, also compared with the extend Kalman filtering method result. The ultrasound measurement validated the estimation method in both trend and major absolutely value of the artery size in different cardiovascular circumstance. In future work, to realize a truly reliable non-invasive system for vascular resistance monitoring, substantial additional validation will be required, likely requiring further system identification procedures to obtain model parameters in an automated fashion.

Chapter 5 Modeling of Peripheral Artery Behavior Subject to Varying Outside Pressure

This chapter describes a 2-D model derived to account for the most prominent features of interaction between underlying tissue and a pair of compliant wearable sensors for peripheral artery monitoring, with outside pressure manipulated by a pressurized cuff on a swine test subject. We compare experimental and modeled output from which variations in relative amplitude of the PVDF and PPG signals are found to show strong correlations with invasively measured systemic vascular resistance (SVR) data in the subject. Finally, we discuss key observations, potential applications, and important limitations of this work, and identify possible future works[41].

5.1. Model for Local Artery and Tissue with Pressure Cuff

Blood pressure and flow along arterial vessels are affected by arterial and tissue properties. The piezoelectric sensor responds predominantly to tangential stress or strain in the PVDF ring as it stretches in response to fluctuations in pressure and volume inside the underlying arteries. However, the pressure experienced by the PVDF ring is not identical to the underlying arterial pressure, due to intervening tissue dynamics. The voltage output of the PPG sensor is, ideally, proportional to the change of the artery's volume. However, due to the varying depth between the photodiode and artery, the illumination of light is also related with tissue dynamics. To approximate this behavior, a simple 2-D model of local arterial and tissue model is used, which to relate outside cuff pressure and artery properties to sensors signals.

The mechanical model used in this work consists of an elastic cylinder for the artery including a linear elastic modulus approximation, other soft tissue and skin approximated as a compressible volume, and a linear cylindrical ring approximation for the sensor, as shown in Fig. 25. The pressure cuff is assumed to a 25mm-radius cylinder, and artery is modeled to a distance of 100mm upstream and downstream from the sensor location. The cuff is wrapped around the foreleg significantly past the artery location on either side. The PPG sensor centered underneath the cuff, and PVDF sensor is 8mm upstream from the PPG above the artery

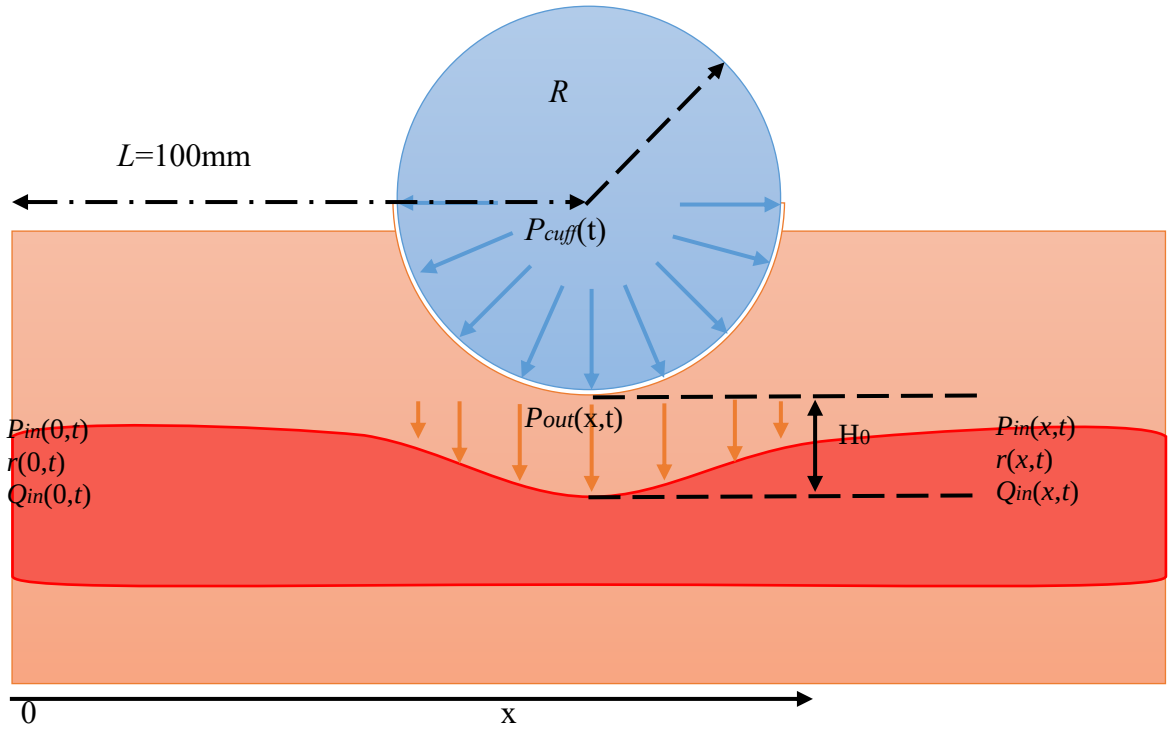

Fig. 23 schematic of swine arm cross scetion alone arterial line

The pressure outside the artery, P_{out} , assuming an approximately cylindrical cuff geometry, is treated as following a single cosine curve along the length of the artery, with peak pressure equal to that inside the cuff. The functional of P_{out} is written as:

$$P_{out}(x,t) = \begin{cases} P_{cuff}(t)\cos\left(\frac{\pi|x-L|}{2R}\right) & ,|x-L| \le R \\ 0 & ,|x-L| > R \end{cases} \qquad (36)$$

Here, x refers to linear distance along the artery and t to time. R is the cuff radius, and L is the position of the midpoint of the cuff along the x-axis.

The tissue between the artery and cuff is approximated by a piecewise-linear model: first, as a linear compressible volume under low to moderate pressures, then as having negligible compression (i.e. solid or rigid behavior) beyond a threshold pressure. Under this hypothesized behavior, distance between the PPG sensor and the artery, HPPG, becomes:

$$H_{ppg}(t) = \begin{cases} H_0 + k[P_0 - \Delta P(L,t)] & , \Delta P(L,t) < P_0 \\ H_0 & , \Delta P(L,t) \geq P_0 \end{cases} \quad (37)$$

$$\Delta P(L,t) = P_{out}(L,t) - P_{in}(L,t) \quad (38)$$

where, H_0 is minimum distance at which the tissue acts as a an incompressible solid, P_0 is the threshold pressure, and k is an effective spring constant for the tissue in the compressible range. $P_{in}(x,t)$ is the blood pressure inside artery.

Similarly, the distance between PVDF sensor and the artery can be written, adjusted just by an 8mm offset along the artery length:

$$H_{pvdf}(t) = \begin{cases} H_0 + k[P_0 - \Delta P(L-8,t)] & , \Delta P(L-8,t) < P_0 \\ H_0 & , \Delta P(L-8,t) \geq P_0 \end{cases} \quad (39)$$

Longitudinally, the arterial vessel is modeled as an elastic cylindrical tube, shown in its lengthwise cross-section in Fig. 22. The viscous effects of blood and vessel are neglected in the present model due to the comparatively short arterial distance examined in this work; rather, emphasis is on distribution of radial artery deformation as a function of position near the sensors. The compliance, C, of the tube is defined as the change in tube cross-sectional area, A, divided by the change in pressure inside the tube, P_{in}:

$$A(x,t) = \pi r(x,t)^2 \quad (40)$$

$$C(x,t) = dA/dP_{in}(x,t) \quad (41)$$

where r is the internal artery radius. From LaPlace's Law for a cylindrical tube, the compliance also can be determined by the geometry of the tube in addition to the elastic modulus of the tube wall:

$$C(x,t) = \frac{2\pi r(x,t)^3}{E(x,t)h} \tag{42}$$

where h is the wall thickness. E, the elastic modulus, increases with the difference between inside and outside pressure. For example, E has been shown to be related to P_{out} and $P_{in}$for arteries [42] as follows:

$$E(x,t) = E_0 e^{\alpha(P_{out}(x,t) - P_{in}(x,t))} \tag{43}$$

where E_0 and $\alpha > 0$ are specific parameters for different individuals and arteries, and E is assumed to only depend on pressure here. By applying conservation of momentum [13], the tube can be modeled as following equations:

$$Q(x,t) - Q(x+dx,t) + \frac{d(Adx)}{dt} = 0 \tag{44a}$$

$$A[P_{in}(x,t) - P_{in}(x+dx,t)] = \rho \frac{dQ(x,t)}{dt} dx \tag{44b}$$

Here, x and t refer to space and time, Q is volume flow rate, and ρ is blood density.

Combining (41) and (44a), the tube model can be rewritten as:

$$\frac{dQ(x,t)}{dx} + C(x,t)\frac{dP_{in}(x,t)}{dt} = 0 \tag{45a}$$

$$A(x,t)\frac{dP_{in}(x,t)}{dx} + \rho \frac{dQ(x,t)}{dt} = 0 \tag{45b}$$

Combining (40) to (45), a nonlinear function relating artery radius to blood pressure and flow, can be obtained as following equations, in discrete form:

$$Q(x,t) - Q(x+dx,t) + C(x,t)[P_{in}(x,t) - P_{in}(x,t+dt)] = 0 \tag{46a}$$

$$Q(x,t) - Q(x,t+dt) + \frac{A(x,t)}{\rho}[P_{in}(x,t) - P_{in}(x+dx,t)] = 0 \quad (46b)$$

$$2\pi r(x,t)[r(x,t) - r(x+dx,t)] = \frac{2\pi r(x,t)^3}{E(x,t)h}[P_{in}(x,t) - P_{in}(x+dx,t)] \quad (46c)$$

$$r(0,t+dt) = r(dx,t) \quad (46d)$$

With known inputs of $P_{in}(0,t)$ and $Q(0,t)$ from invasive catheterization, as well $P_{out}(x,t)$ from digital pressure gauge, the discrete equation (46) can be numerically solved with an initial value $r(0,1)$. The integration steps are chosen as $dx = 0.1\text{mm}$ for space and $dt = 0.005\text{s}$ for time, the latter the same as the experimental sampling time.

The voltage output of the PPG and PVDF sensors are modeled as:

$$U_{ppg}(t) = K_{ppg}H_{ppg}(t)\int f_1(t)\pi r(L,t)^2 L_{ppg}dt \quad (47)$$

$$U_{pvdf}(t) = K_{pvdf}\int f_2(t)d_{31}E_1A_1\{1 + \frac{[2r(L-8,t)+H_{pvdf}(t)]}{R_{arm}}\}dt \quad (48)$$

where K is the gain for the respective sensor, f_i is the transfer function of any electronic filters, and L_{ppg} is the length of the artery segment directly under the PPG sensor, assumed to be constant. E_1 is the elastic modulus of PVDF, $A_1$is the surface area of the PVDF and d_{31} is the PVDF piezoelectric strain coefficient. The total radius of the limb is a constant value, R_{arm}.

5.2. Model Parameters

Representative values from the literature[43][44][45] were selected as approximate values, as listed in Table I. In addition, the elastic modulus parameters E_0 and α in (43) are observed to vary substantially before and after NE infusion, and thus were estimated individually by optimizing the fit between the measured sensors signals and the simulated signal. The first cuff pressure tests with or without NE infusion were used to calibrate the parameters.

Table 5 Model parameters for local artery and tissue with pressure cuff

Variable			
Nominal values used throughout testing:	Parameter	Value	Units
		$r(0,1)$	
R_{arm}	initial artery radius	1.5	mm
E_1	limb radius	50	mm

t	sensor modulus	2.5		GPa
d_{31}	PVDF thickness	52		μm
K_{ppg}	piezoelectric coefficient	11×10^{-12}		C/N
K_{pvdf}	gain of PPG	2000		
ρ	gain of PVDF	200		
L	blood density	1060		kg/m3
H_0	location of cuff	100		mm
k	initial distance	2		mm
R	tissue spring constant	1.12×10^{-2}		mm/mmHg
Identified from first test, used in two further testing:	cuff radius	25		mm
E_0		w/o NE	w NE	
α	elastic modulus	8.4	10.2	kPa
P_0	rate of elasticity to blood pressure	10	12.5	kPa/mmHg
P_0				mmHg

5.3. Experimental setup and signal preparation

A swine test subject was anesthetized for cardiovascular testing, and maneuvers were performed subject to University of Michigan animal protocol. Arterial blood pressure (ABP), cardiac output (CO) and volumetric flow were tracked invasively using pulmonary artery catheterization.

A polyvinylidene difluoride (PVDF) pressure sensor and a photo plethysmogram (PPG) were placed on the same swine foreleg next to each other. The sensors were covered by an air-filled cuff, which controlled the surface pressure on swine foreleg when supplied from an air pump and valve. The air pressure inside the bag was measured by a 1.2 MPa pressure transducer. All signals were collected and stored using a BIOPAC MP150 data logging system and analyzed retrospectively.

After completion of testing, SVR was computed from cardiac output and mean arterial pressure. Changes in SVR were induced by periodic infusion of norepinephrine (NE), with SVR increasing during infusion and decreasing when each infusion stopped. The infusion flow rate is manually controlled by a valve with a constant NE concentration. The experiment result shows that both arterial pressure and SVR were increased with NE infusion. The experimental data analyzed in this paper included one NE infusion start/stop with six cuff pressure tests. The first

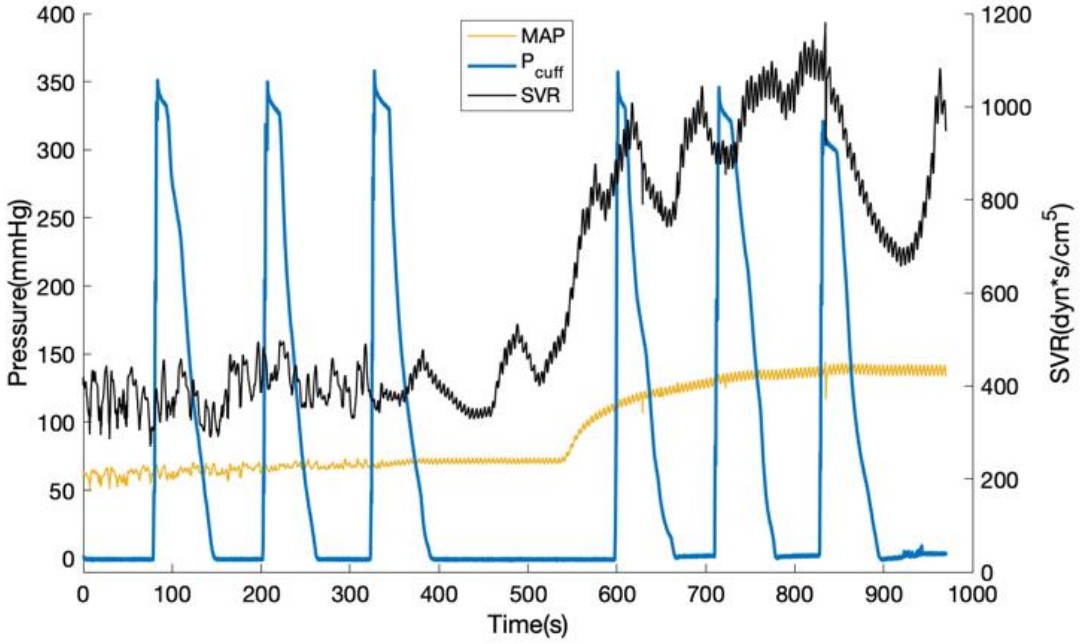

Fig. 24 systemic vascular resistance (svr) and mean arterial pressure (map) changes with norepinephrine, and cuff pressure trajectories

three cuff tests were done prior to NE infusion, and the remaining three tests were done during NE infusion, as shown in Fig. 26.

For each cuff pressure test, the cuff was inflated then air in the cuff was slowly released using a valve, such that pressure dropped continuously from 350mmHg to 0mmHg. Qualitatively, there appeared to be some repeated sensor dynamic characteristics during repeated cuff deflation at a given SVR level. However, both PVDF and PPG sensor signals were observed to undergo significant changes with the increase of SVR and blood pressure for given cuff pressures. Fig. 27 and Fig. 28 shows sample trajectories of sensor signals and cuff pressure with and without NE infusion, respectively. In this study, we explore in more depth the factors contributing to the amplitude of the sensors signals for each blood cycle, with respect to external cuff pressure.

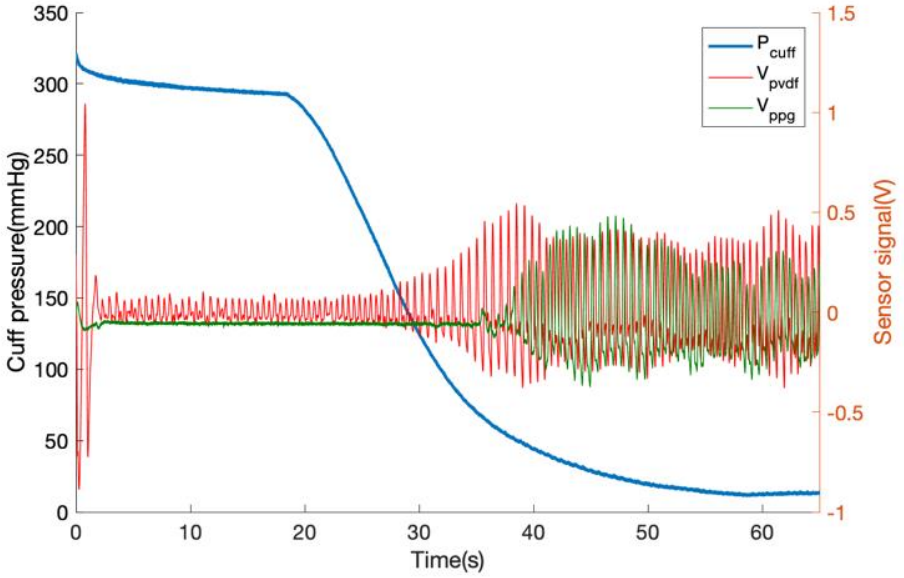

Fig. 25 : sample experimental signal and cuff pressure trajectories without norepinephrine infusion

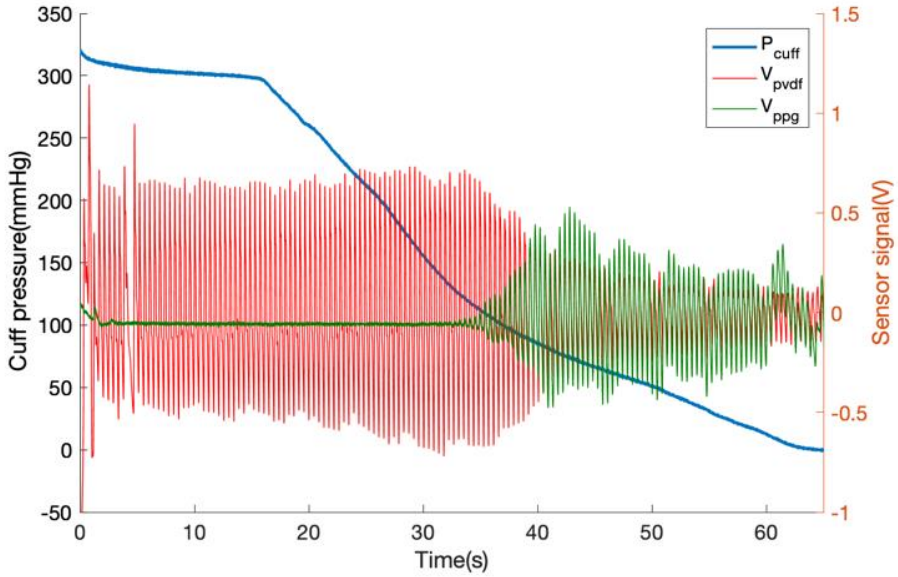

Fig. 26 sample experimental signal and cuff pressure trajectories without norepinephrine infusion

5.4. Model results

Results after model fitting are shown in Fig. 23 and Fig. 24, showing experimental and modeled sensors signals amplitude as a function of applied external cuff pressure. Tests 1-3 (red) were the tests without NE infusion, with 53±2 mmHg diastolic pressure and 73±2 mmHg systolic pressure. Tests 4-6 (turquoise) were the tests with NE infusion, with 119±1 mmHg

diastolic pressure and 157±3 mmHg systolic pressure. Once identified for a sample test, the model provides quantitively prediction in the signals' responses to the same animal when there are not other interventions altering cardiovascular function (i.e., for the nominal cardiovascular condition captured in the red curve). In contrast, a significant change in the arterial dynamics and sensors signals are observed after norepinephrine is infused, suggesting possible origin of major signal changes in response to changes in cardiovascular and vascular behavior.

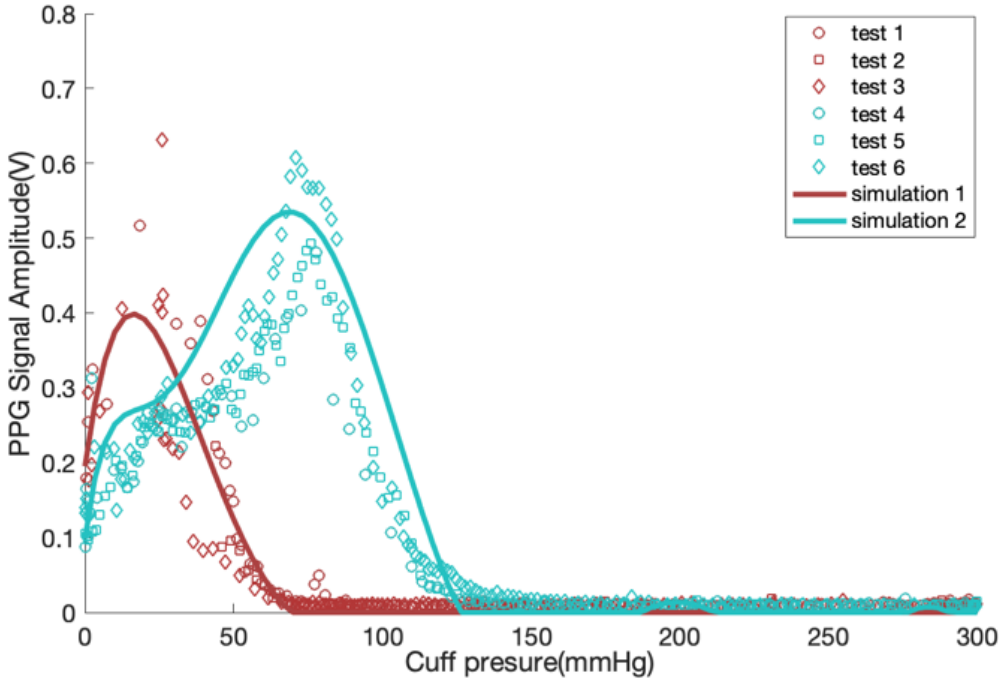

Fig. 27 experimental and modeled ppg sensor signal amplitude respect to cuff pressure

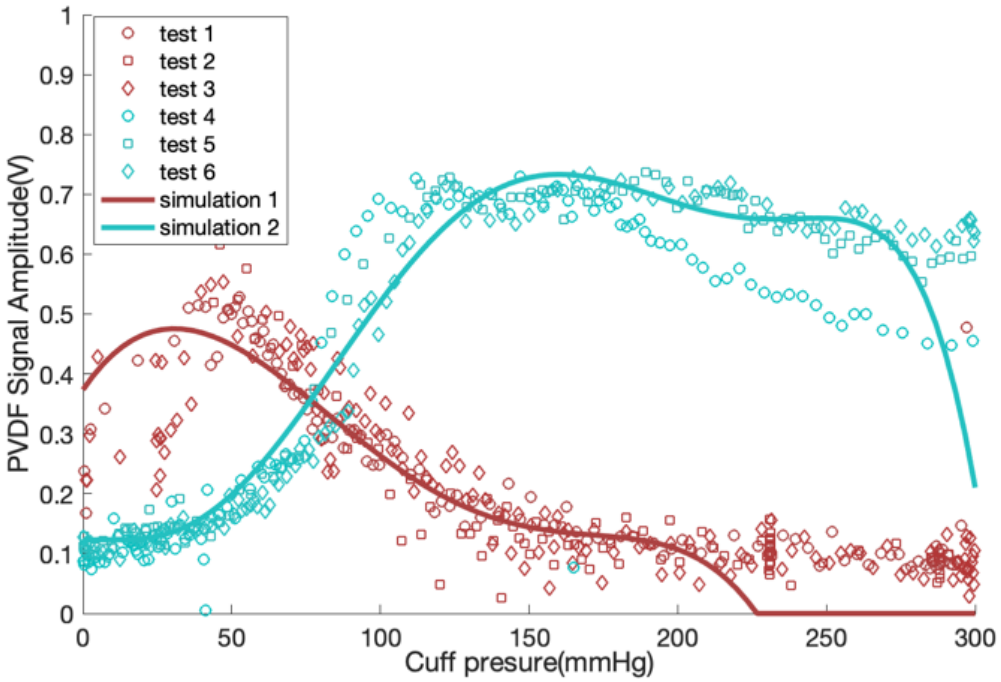

Fig. 28 experimental and modeled pvdf sensor signal amplitude respect to cuff pressure

The peak amplitude of the PPG signal is observed when cuff pressure is below diastolic pressure, which can be explained by tissue dynamics in the model. Meanwhile, the PPG signal is close to zero when cuff pressure is higher than systolic pressure, as would be expected. The PVDF signal amplitude reaches its maximum with the cuff pressure close to diastolic pressure. This is consistent with maintaining a large proportional change in strain at the PVDF sensor when accounting for compression of the tissue, though the degree of agreement given the sensor's offset location may be partly coincidental.

Results from Fig. 29 and Fig.30 are consistent with previously proposed methods for tracking changes in vascular resistance, which found that variations in relative amplitude and hysteresis between the PVDF and PPG signals to show strong correlations with invasively measured SVR . In those experiments, sensing ring tension was adjusted to maximize amplitude of the PVDF signal, which in this case is 50mmHg in cuff pressure, slightly below diastolic pressure prior to NE infusion. During NE infusion, the SVR increases from 413 ± 53 dyns $\cdot$ s/cm^5 to 956 ± 150 dyns $\cdot$ s/cm^5 with NE infusion. In this process, the amplitude of PVDF signals decreases significantly, from 0.5 to 0.15 V, as reduction in peripheral arterial radius results in much reduced motion transmission to the PVDF material, especially when accounting for tissue

compressibility. Meanwhile, the PPG signal in fact increases, from 0.1 to 0.3, reflecting larger proportional change in artery radius only as observed by the optical sensor.

Moreover, the cuff pressure affects the local pulse transit time (PTT) between the two sensors. With more faster cuff pressure, the peripheral vascular resistance increases and the PTT decreases, but less than 1ms. Meanwhile, there is no significant effect on PTT from ECG to peripheral as cuff pressure changes. The PTT does change in both cases with norepinephrine infusion.

5.6. Conclusion

In this chapter, a 2-D model is proposed that may be useful for tracking changes in peripheral artery behavior when using a photo plethysmograph (PPG) sensor and a piezoelectric (PVDF) sensor under a pressure-varying cuff. A simple mechanical model for local artery and tissue captures broad features of the PPG and PVDF signals amplitude during cuff deflation cycles. Results show possible systolic pressure estimation with PPG sensor and diastolic pressure estimation with proper-located PVDF sensor. Perhaps more importantly, changes in sensor response to external pressure variation may allow changes in arterial properties (elasticity parameters, radius) in response to medical interventions to be inferred. Observed behavior is also consistent with systemic vascular resistance (SVR) tracking performed in previous works.

Naturally, there are several limitations in this study as performed at this time. First, the proposed tissue model oversimplifies the complex structure of bone and skin adjacent to peripheral artery, and thus cannot capture all details of tissue and sensor behavior. This is most clearly seen in the additional complexity of experimental vs. modeled sensors signals. Moreover, the model also neglects viscoelastic behavior in artery wall, while in reality there is likely to be. The largest limitation of the current work is the small number of tests and the single subject, with short monitoring periods.

Chapter 6 Feedback Model for Systemic Hemodynamic

In this chapter, we propose that tracking vascular resistance in combination with heartrate can provide substantial insight into cardiovascular response to clinical interventions, at least under very controlled circumstances. We hypothesize that a new systemic hemodynamic model incorporating peripheral vascular resistance feedback would be able to reproduce oscillatory trajectories that appear to arise from different timescales of response to medication, and identifiable changes in the system. Experimental results in swine indicate that the model provides the ability to generate a closed-loop response for mean-arterial pressure due to an intervention – norepinephrine infusion – that is suggestive that feedback mechanisms were captured in approximate terms.[46]

6.1. Systemic Hemodynamic Feedback Model

Blood pressure is controlled though multiple physiological mechanisms, with two major mechanisms being the vascular resistance, estimated from the wearable sensor, and heartrate (HR). Transfer functions between blood pressure, heartrate, and vascular resistance are identified during perturbations to cardiovascular function by vasopressor infusion (norepinephrine), in varying sequences, and controlled hemorrhage. The norepinephrine is assumed to be able to induce changes in both heart rate and vascular resistance as an input signal to the full cardiovascular system, while the animal's compensation to blood pressure changes is modeled as a feedback loop to both mechanisms.

Our proposed model (shown in Fig. 31), includes four time-varying signals. These represent the norepinephrine infusion, $N(s)$, heart rate, $H(s)$, peripheral vascular resistance, $R(s)$, and mean arterial pressure, $P(s)$, each produced by a partial model of systemic circulation and hemodynamic compensation mechanisms. Transfer functions are used to represent of set a linear, time- invariant dynamics between the variables, identified experimentally. The peripheral vascular resistance and heart rate respond to changes in both norepinephrine infusion rates and blood pressure (left two blocks), and those two signals regulate blood pressure through the system "plant" (right block). *H(s)*, *R(s)* and *P(s)* can be found using Laplace transform from the

time-domain measurements: heart rate and PVR were obtained from the nonlinear local artery model and non-invasive sensors, while arterial pressure was from invasive measurements. Additionally, the *N(s)* was qualitatively estimated from zero to one, meaning infusion stop and maximum infusion speed using valve position, due to a lack of direct flow measurement in the experimental setting.

The parameters of the open-loop transfer functions are identified with the first set of NE infusion test data before and after hemorrhage, separately, by minimizing the sum of squared errors of the model output and measurement. The orders of the transfer functions were selected based on the percent overshoot and settling time. Heart rate dynamics presented as an overdamped system with no overshoot, acting as though subject to a step input. Meanwhile, the PVR and BP dynamics showed large overshoot with a longer settling time, which could typically be represented by a 3rd-order underdamped system.

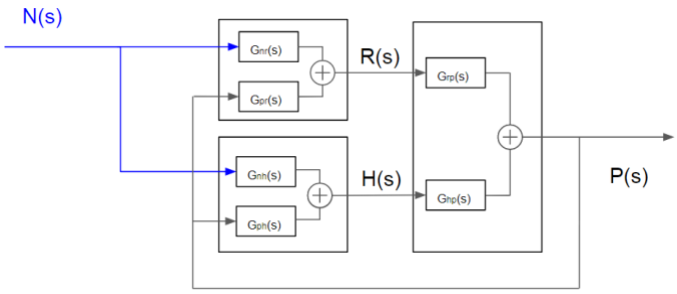

Fig. 29 Feedback model proposed for blood pressure response to norepinephrine infusion

6.2. Simulation Result

The result from model fitting is shown in Fig. 32 and Fig. 33, showing experimental and modeled changes in heartrate (pink), vascular resistance (blue), and blood pressure (yellow) from the sequence of norepinephrine infusion profiles (black, approximate) before and after hemorrhage. The simulation result and measurement were normalized by the maximum value of heart rate and arterial pressure, 200 bpm and 180 mmHg, respectively.

It is found that 2nd-order models for heart rate dynamics and 3rd-order models for other transfer functions are effective in capturing signal fluctuations. After model order reduction, the model hardly captured the dynamics of blood pressure and heart rate. Once identified for a sample norepinephrine infusion, the model continues to provide reasonable accuracy in predicting the signals' responses in future infusions applied to the same animal, without other interventions

altering cardiovascular function. In contrast, a significant change in the arterial dynamics is observed after hemorrhage is performed. Importantly, regulatory feedback blocks remain approximately constant when re-identified after hemorrhage, with changes in the identified model occurring predominantly in the "plant," or model for blood pressure dynamics. Fig. 32 shows that the model's response to NE infusion variations before the hemorrhage were close to the measurement from the upper raw plots, while the lower plots shows the mismatches between blood pressure and PVR. Similar result can be observed in Fig. 33, with the transfer functions estimated after hemorrhage test failing to predict the behaviors before hemorrhage.

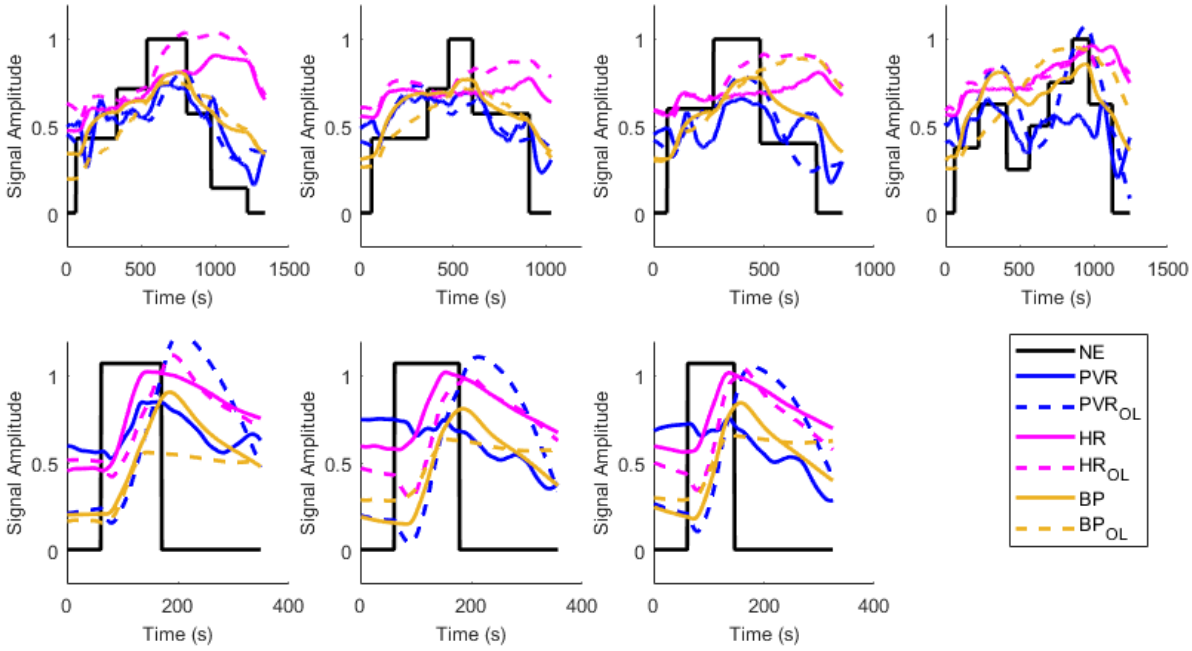

Fig. 30 Sample experimental and modeled signal trajectories during norepinephrine infusion using model fitting before hemorrhage.

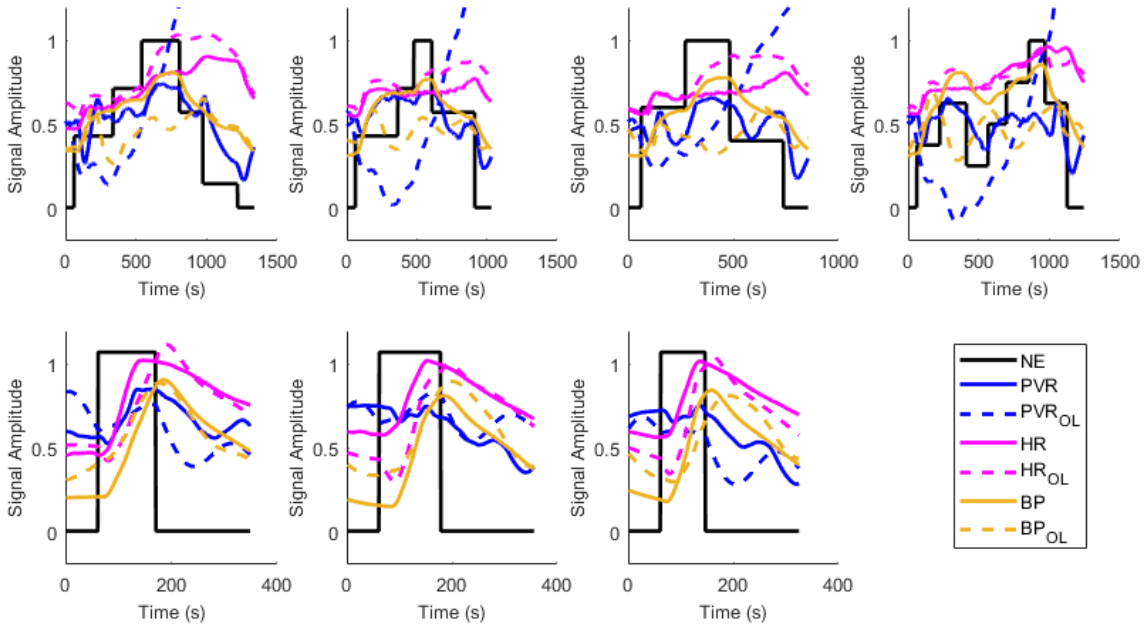

Fig. 31 . Sample experimental and modeled signal trajectories during norepinephrine infusion using model fitting after hemorrhage.

6.3. Pole-zero Analysis of Different Medical Interventions

A pole-zero analysis was performed on the identified dynamics to interpret observed behavior in a traditional control systems framework. The pole-zero analysis are illustrated in Fig. 34 and Fig. 35, where the left plot shows the pole-zero plots for (left) peripheral vascular resistance dynamics ($N(s)$ and $P(s)$ to $R(s)$; (middle) heart rate dynamics ($N(s)$ and $P(s)$ to $H(s)$); and (right) blood pressure dynamics ($N(s)$ and $H(s)$ to $P(s)$. Each of the dynamic including two transfer functions, and the pole-zero were the roots of the numerator and denominator of two polynomials (blue and yellow).

All of the transfer functions poles have negative real parts, and the dominant poles of PVR and blood pressure transfer functions are very close to imaginary axis. Thus, those two systems can be interpreted under damped systems. The dominant poles move away from the real axis after hemorrhage, which indicates that the hemodynamic became more under damped and easier to oscillate with an input signal. This meanwhile, a positive zero occurred after hemorrhage which makes the PVR response unstable if applied as the model to the before-hemorrhage case, shown in Fig. 31 upper row plots.

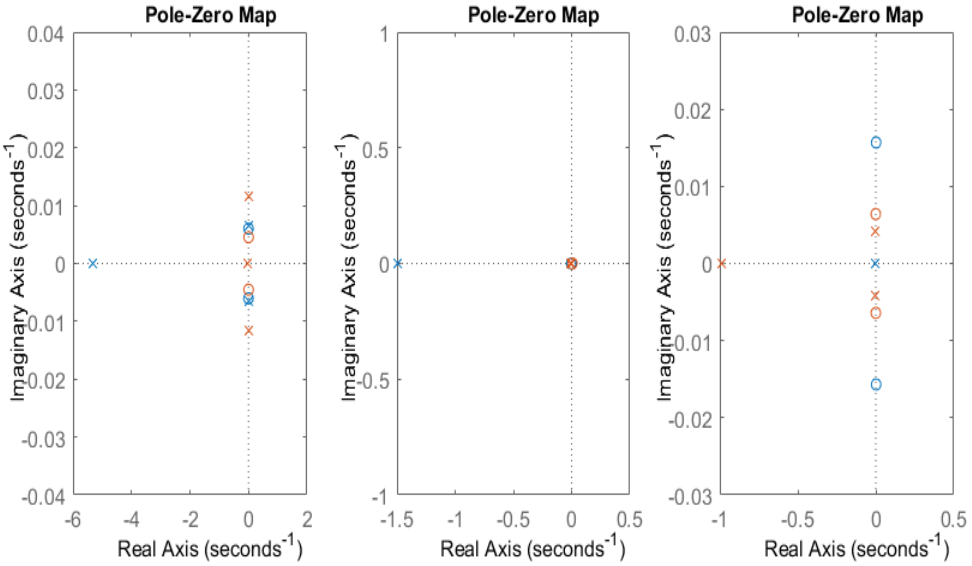

Fig. 32 Pole-zero map of hemodynamics before hemorrhage

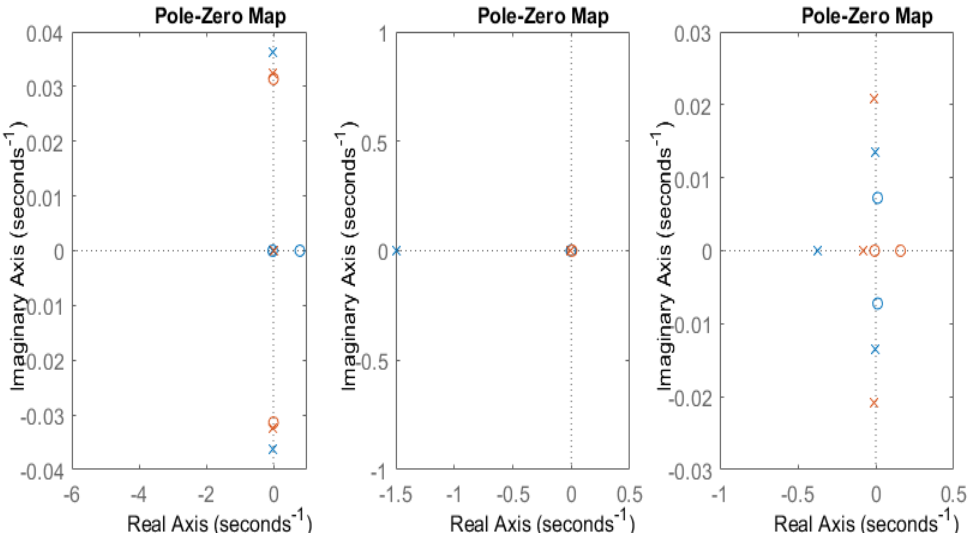

Fig. 33 Pole-zero map of hemodynamics after hemorrhage.

6.4. Conclusion

Results from the combination of local peripheral arterial radius modeling and empirical systemic feedback modeling appear to permit insight into the interrelationship of feedback mechanisms during cardiovascular compensation. The results shown at present provide only indirect validation of models, but the ability to generate a closed-loop response for mean-arterial pressure due to an intervention – norepinephrine infusion – is suggestive that feedback mechanisms are at least being captured in approximate terms.

Naturally, there are many limitations on this study as performed at the current time. First, norepinephrine infusion rates are recorded in only approximate terms, as exact rate of flow was not available from the test setup. Inaccuracy of norepinephrine infusion rate may limited the parameter identification of the transfer functions, though it should not undermine the method and results. More importantly, simulations were found to be very sensitive to proper initial value selection, done manually at this time, representing a limitation on model implementation at this time. Furthermore, though we attribute observed behaviors to only two specific feedback mechanisms (heart rate and vascular resistance), the empirical model fitting may cause other compensatory mechanisms, if present, to be conflated with the measured signals.
Feedback modeling at this stage of development additionally does not seek to identify physiological origins for the dynamics, i.e. 2nd-order vs. 3rd-order responses in the feedback dynamics model, or the fluid flow origins of the blood pressure dynamics. In addition, stability and robustness of the feedback model constructed from identified transfer functions could receive more thorough study, as these results are limited to tests with specific bounded inputs and bounded outputs.

Findings from this work suggest that tracking vascular resistance in combination with heart rate can provide substantial insight into cardiovascular response to clinical interventions, at least under very controlled circumstances. The proposed sensing technology appears to provide a rapid, detailed response to interventions known to alter arterial behavior. Significant results include the ability to reproduce oscillatory trajectories that appear to arise from different timescales of response to medication, and identifiable changes in the system "plant," i.e. blood pressure response to regulatory mechanisms, after hemorrhage. However, additional validation experiments would be required to fully understand the physiological origins of the dynamics identified in this work, or to fully confirm the observed behaviors' attributions among those mechanisms, as they may be conflated with other cardiovascular compensation mechanisms, or susceptible to model over-fitting.

Chapter 7 Prediction of Hemodynamic Decompensation with the Systemic Model and EKF

This chapter describes a simple feedback model for cardiovascular autoregulation in human subjects, describes how feedback signals were tracked, and performs parameter and state estimation for hemodialysis patients. Certain estimator error behaviors will be associated with later decompensation during hemodialysis. This work seeks to isolate various components of cardiovascular autoregulation to construct models of interacting feedback dynamics. Over time frames of minutes to hours, major feedback signals regulating BP are considered to include heartrate, compression volume, and peripheral vascular resistance. Importantly, existing sensing systems for continuously measuring peripheral vascular resistance are available on a continuous basis only in specialized clinical settings. Our proposed sensor provides an opportunity to more readily perform continuous vascular resistance tracking, and also provides high-fidelity tracking of small peripheral artery pressure fluctuations, which we have also proposed for analysis in predicting IDH or assessing other cardiovascular events such as hemorrhage.

Here, we hypothesize that incorporating peripheral vascular resistance into feedback models for cardiovascular autoregulation can increase understanding of decompensation and improve IDH prediction. This effort differs from previous attempts to model feedback dynamics primarily in the availability of additional feedback signals from non-invasive sources, and also the examination of variation in feedback over time during the complex medical intervention of hemodialysis.[47]

7.1. Systemic Feedback Model

The body's ability to compensate against stress caused by trauma, illness, and disease can substantially complicate diagnosis and detection of complications in many situations. For example, multiple autoregulatory feedback loops exist to maintain blood pressure at the core and vital organs. As a result, measurements of blood pressure tend to act as a trailing indicator of cardiovascular distress, while feedback behaviors that are much more difficult to monitor may be changing rapidly. Here, the candidate hypothesize that incorporating peripheral vascular resistance into feedback models for cardiovascular autoregulation can increase understanding of decompensation and improve IDH prediction. This effort differs from previous attempts to model feedback dynamics primarily in the availability of additional feedback signals from non-invasive sources, and also the examination of variation in feedback over time during the complex medical intervention of hemodialysis. The feedback model used for IDH prediction was constructed from a simple nonlinear cardiovascular monitor and a set of linear low-pass filters representing feedback processes. While a major simplification of full cardiovascular dynamics, the selection of models was intended to balance the range of autoregulatory phenomena to be monitored with the number of parameters to be identified.

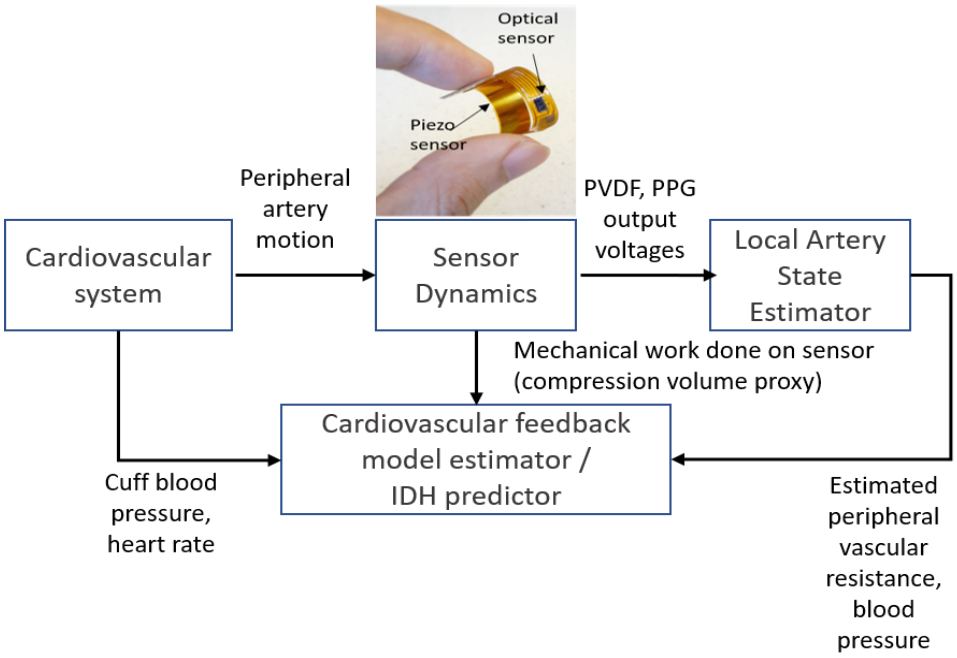

Fig. 34 Conceptual framework for decompensation prediction during hemodialysis: signals associated with blood pressure autoregulation are monitored directly or indirectly using a simple wearable sensor and used to identify parameters in an abstracted model for feedback processes within the body; signals from the estimator are used to predict later decompensation.

The cardiovascular system was modeled as a simple fluidic resistance and capacitance driven by a pressure source, with resistance and input pressure influenced by "control inputs" of heart rate, u_1, mechanical work done per beat by the artery to the sensor (a proxy for compression volume), u_2, and peripheral vascular resistance, u_3, contained in vector **u**:

$$\dot{P} = f(P, \mathbf{u}, d) = l_1 u_1 u_2 - l_2 \frac{P}{u_3} + l_3 d \quad (49)$$

where *P* is blood pressure as would be measure using a conventional blood pressure (BP) cuff or arterial line; l_1 is a parameter to scale the combined pressure forcing input of heart rate and supposed compression volume; l_2 is a parameter for first order dynamics produced by total hemodynamic capacitance and resistance, assumed to be inversely dependent on peripheral vascular resistance; and d is a net disturbance from external factor (activity level, hemodialysis effects, etc.).

Feedback dynamics were modeled as responding to the difference between blood pressure and some supposed internal reference pressure, P_r, with a time delay represented as a linear low-pass filter. In addition, the disturbance was assumed to be able to affect the feedback signals directly, with comparable response time. The resulting simple feedback model becomes, in Laplace space,

$$U_i(s) = \frac{b_i}{s+a_i}(P_r - P(s)) + \frac{c_i}{s+a_i} D(s) \quad (50)$$

where bi is the feedback gain to pressure, a_i is the first-order filter parameter, and ci is the coupling parameter to external disturbance for the i-th control input.

Measurements y_1, y_2, and y_3 were assumed to be available for each of the three feedback signals, though fidelity and sampling rate could differ based on source of measurement, as described in more detail in Section III. In addition, a measure of BP, y4, was assumed to be at least intermittently available. The resulting feedback system with measurement locations is summarized in block diagram form in Fig. 37.

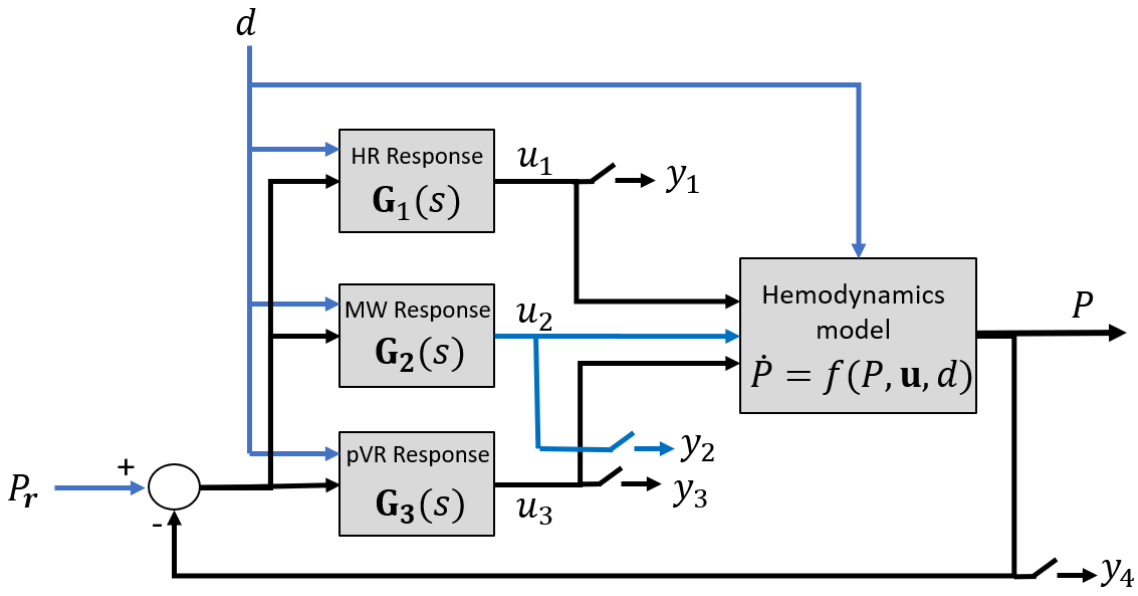

Fig. 35 Individual low-order approximations of cardiovascular behavior are connected via feedback between blood pressure variation and supposed autoregulatory (i.e. feedback control) signals.

7.2. Experimental Setup and Signal Processing

Peripheral arterial behavior was monitored using sensor data from a PPG sensor and the compliant piezoelectric polymer (polyvinylidene difluoride, or PVDF) sensor worn on the fingers. Details of PVDF sensor design and usage for tracking peripheral vascular resistance have been previously reported in swine subjects in Chapters 4 and 5. In addition to wearable sensor information, conventional cuff blood pressure (BP) was recorded approximately every 15 minutes.

Sensors were applied to 110 hemodialysis patients in the inpatient dialysis unit at the University of Michigan Hospital, from which 91 complete data sets were successfully collected; 50 data sets have been fully processed at the time of writing and are reported on in this manuscript. The PVDF ring was applied within approximately ten minutes of the beginning of hemodialysis, and ring tension was adjusted manually to produce a clear PVDF waveform. For some patients, readjustment was performed if the sensor was dislodged due to patient activity. Other than those cases, both patients and care providers were kept blind to signal behavior during

the dialysis session. All data collection was performed under IRB-approved human subject protocol UM HUM00112816.

Raw voltage versus time data from the PVDF and PPG sensors was processed to provide measures of relative change in major autoregulatory cardiovascular behaviors. First, heart rate (labeled HR) was extracted from peak values of the PPG signal. Second, a measure was sought to approximate compression volume at the heart. A proxy was selected as the mechanical work (labeled MW) done by peripheral arterial motion on the PVDF ring within each cardiac cycle. This is only hypothetically related to cardiovascular health but chosen as at least partially representative of the heart's work capacity during individual heartbeats. Third, peripheral vascular resistance (labeled pVR for conciseness, not to be confused with pulmonary vascular resistance often labeled PVR) was estimated using methods previously in chapter 4.

It is important to note that peripheral vascular resistance estimation has not yet been previously validated on human subjects, so a major assumption in this work is that the methods applied to swine subjects would translate to humans. In brief, a simple model for tissue viscoelasticity between the artery and PVDF and PPG sensors is identified using a fast-time-scale (200 Hz sampling rate) extended Kalman filter (EKF) to produce state estimates of changes in local artery radius and internal blood pressure. pVR changes are derived from radius change. This approach has shown good agreement (<5% average absolute error) between estimated vascular resistance changes and those measured by gold standard arterial catheterization in swine [10].

An adjustment to prior methods done in this work was to adjust sensor noise weighting fort the local artery model EKF based on pulse transit time (PTT) between PPG and PVDF locations. When PTT was within a specified margin, PVDF and PPG signals were incorporated into the EKF as normal. When PTT deviated from the expected margin, one or both the sensors was assumed to be disturbed by patient movement, and the EKF was applied during that cardiac cycle based on a substantially increased noise variance (i.e., placing substantially greater trust in the model vs. measurements).

For each subject, proposed feedback signals were normalized to a 0 to 1 scale based on a set maximum (subscript max) and minimum (subscript min) plausible range for those signals, to simplify scaling between parameters.

$$y_1 = \frac{HR - HR_{min}}{HR_{max} - HR_{min}} \tag{51}$$

$$y_2 = \frac{MW - MW_{min}}{MW_{max} - MW_{min}} \tag{52}$$

$$y_3 = \frac{\widehat{pVR} - pVR_{min}}{pVR_{max} - pVR_{min}} \tag{53}$$

where y_1 is the normalized magnitude of heartrate, y_2 is the normalized magnitude of work being transmitted to the compliant sensor, and y_3 is the normalized magnitude of peripheral vascular resistance calculated by the local artery model EKF. Average values for the first 30 seconds for measured signals were used as initial conditions where relevant during further parameter identification.

A byproduct of the peripheral vascular estimation process is to provide a continuous estimate of blood pressure (BP). While the PVDF sensor cannot directly measure blood pressure, an internal state in the vascular resistance model is the fluctuation internal artery pressure over time. While vulnerable to long term drift, when provided with a reference BP measurement (i.e. from a BP cuff), the sensor and estimator have been found to track BP measured by conventional means, Pcuff, with approximately 10% error over a time period of several hours. This lower-confidence measure, $\hat{P}_{pVR}$, was used to supplement intermittent cuff BP measurements in later cardiovascular model state estimation, as BP output, y4:

$$y_4 = \begin{cases} P_{cuff} + v_{4,cuff}, & P_{cuff} \neq 0 \\ \hat{P}_{pVR} + v_{4,\,pVR,} & P_{cuff} = 0 \end{cases} \tag{54}$$

where v4 is a measure of noise or accuracy error in the signals, varying with the source (cuff vs. pVR estimator).

Finally, "disturbance", d, to the cardiovascular system was treated as being partially generated by activity level. A crude approximation of patient activity level, labeled $\bar{d}$, was taken from the unfiltered mean PVDF amplitude as computed from a rolling averaged of 30 seconds, as large amplitude variations in PVDF output are associated with motion artifacts. Standard deviation of the PVDF signal over that period was used to compute a disturbance variance for the cardiovascular feedback model state estimator, as described in the following sections.

7.3. Parameter Identification and State Estimation

Parameter identification and state estimation were done simultaneously using an augmented extended Kalman filter. First, dynamics in (49) and (50) were converted to discrete time with

states collected in state vector $\mathbf{q} = [P \ u_1 \ u_2 \ u_3]^{\boldsymbol{T}}$. Unknown parameters from (49) and (50) were collected in a parameter vector,

$$\boldsymbol{\theta} = [P_r \ \lambda_1 \ \lambda_2 \ \lambda_3 \ \alpha_1 \ \beta_1 \ \gamma_1 \ \alpha_2 \ \beta_2 \ \gamma_2 \ \alpha_3 \ \beta_3 \ \gamma_3]^T \tag{55}$$

where λ1, λ2, and λ3 are discrete-time analogs to l1, l2, and l3 from (49), and αi, βi, and γi terms are discrete-time analogs to ai, bi, and ci from (50). State and parameter vectors were combined to create a single plant model for the estimator based on estimated states, $\hat{\mathbf{q}}$, and estimated parameters, $\delta\hat{\boldsymbol{\theta}}$, where δ indicates that parameters are estimated as their perturbation from a set of nominal baseline values:

$$\begin{bmatrix} \hat{\mathbf{q}}^{\mathbf{0}}(k+1) \\ \delta\hat{\boldsymbol{\theta}}^0 \ (k+1) \end{bmatrix} = \begin{bmatrix} f(\hat{\mathbf{q}}(k), \hat{\boldsymbol{\theta}}(k), \bar{d}(k)) \\ \alpha\mathbf{I} \cdot \delta\hat{\boldsymbol{\theta}}(k) \end{bmatrix} \tag{56}$$

Here, α is a decay parameter; conceptually, parameters are being treated as though they slowly perform a random walk around their nominal values driven by external disturbances, to be tracked by this augmented EKF.

Given the measurements identified in (56), the output vector of the physical system is simply

$$\mathbf{y} = \mathbf{q} + \mathbf{v} \tag{57}$$

where **v** is a vector of the noise in each measurement, and thus the estimated system output is simply $\hat{\mathbf{y}} = \hat{\mathbf{q}}$.

A state and parameter updates are then generated in the common observer form

$$\begin{bmatrix} \hat{\mathbf{q}}(k+1) \\ \delta\hat{\boldsymbol{\theta}} \ (k+1) \end{bmatrix} = \begin{bmatrix} \hat{\mathbf{q}}^{\mathbf{0}}(k+1) \\ \delta\hat{\boldsymbol{\theta}}^0 \ (k+1) \end{bmatrix} + \mathbf{L}(\hat{\mathbf{y}}(k) - \mathbf{y}(k)) \tag{58}$$

where **L** is a gain matrix calculated by existing extended Kalman filter methods based on linearization of dynamics in (56) about the current state estimates and iterative generation of error covariance and estimator gain matrices.

7.3. Peripheral Vascular Resistance Observations

Before discussing feedback model estimator results, it is useful to describe representative behavior of peripheral vascular resistance tracking as implemented based on the authors' previous methods from chapter 4. It was observed that consistency of inferred peripheral vascular resistance alone was a strong negative predictor of intradialytic hypotension. Among patients where inferred vascular resistance varied less than ±50%, only 5% of sessions resulted in substantial decompensation (set as a drop >25% of nominal BP) and/or had patient reported symptoms of distress. In contrast, over 30% of cases with large vascular resistance fluctuations were associated

with a drop in BP and over 30% with reported symptoms (some cases overlapping). Examples of patients with small and large inferred vascular resistance changes are shown in Fig. 38 with corresponding BP fluctuations.

Our interpretation of these observations is that fluctuations in peripheral vascular resistance may be indicative of compensatory response that will eventually result in decompensation, but vascular resistance change alone is not necessarily tied to decompensation. Rather, vascular

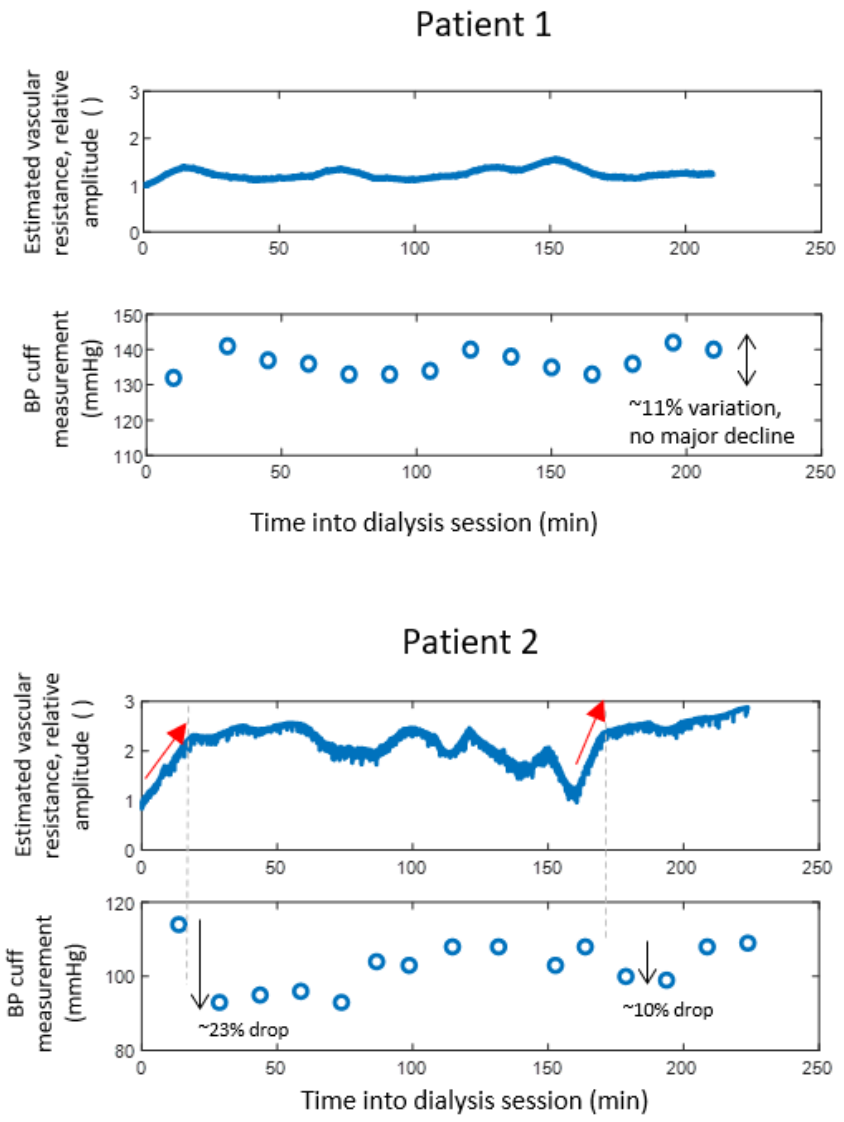

Fig. 36 Mild variation in inferred or estimated peripheral vascular resistance, as in Patient 1 above, is very rarely associated with large BP fluctuations, while large patients experiencing large BP tend to exhibit prior peripheral vascular response, as in Patient 2 above.

resistance change may also occur as part of a compensation process that is sustainable, at least over the several-hour period of a hemodialysis session, or as a response to other disturbances, such as change in activity level. The need to distinguish unsustainable compensatory response from other cases where PVR fluctuated thus partially motivated the feedback modeling described above.

7.5. Estimator Design and Representative Outputs

Several items were calibrated in the model and extended Kalman filter using an initial training set of 20 patients (from 50 overall). These included the selection of 30 seconds for averaging of PVDF noise to compute $\bar{d}$ and nominal values for $\boldsymbol{\theta}$. Rolling average duration was selected to minimize mean absolute error in $(\hat{\mathbf{y}} - \mathbf{y})$ for this training data set, while nominal values for $\boldsymbol{\theta}$ were set based by a brute force search to minimize total absolute error $(\hat{\mathbf{y}} - \mathbf{y})$ across all 20 subjects with a single set of values, as a starting point from which parameters would then diverge on an individual basis during EKF application.

Fig. 39 shows a sample set of estimation results for a patient with significant BP variation but without decompensation (BP remained above that at the beginning of hemodialysis). The estimator is only modestly effective in predicting blood pressure trends, with errors up to 30 mmHg, when comparing estimates for pressure to the intermittent cuff measurements. This is likely because the disturbances that may be perturbing blood pressure are largely unknown. However, the feedback signals are much more closely predicted by the estimator. This is in part due to substantial autocorrelation of those

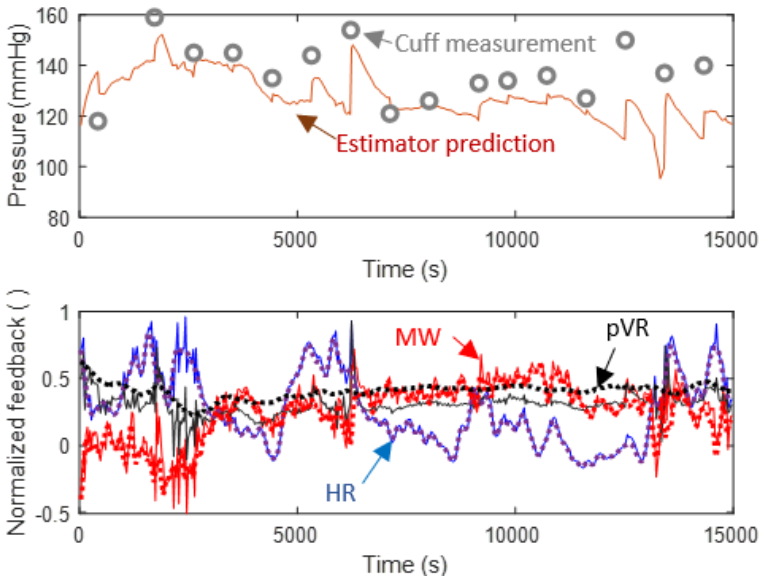

Fig. 37 Blood pressure predictions from the EKF provide only modest tracking of trends in BP during hemodialysis, as for this sample patient, though feedback signals are more effectively predicted (solid: from EKF; dashed: from physiological sensing). BP prediction errors tend to be associated with sustained error between prediction and measurement of one or more of the feedback signals.

signals with themselves, but also aided by the continuous feedback measurements and their interrelationship. Notably for the sample patient in Fig. 39, "overperformance" of BP relative to the model in the latter portion of hemodialysis is associated with an "overperformance" of one of the feedback signals: in this case peripheral vascular resistance remained higher than anticipated by the estimator based on feedback parameters being identified since the start of the session.

To further evaluate apparent feedback effectiveness, a control chart-like analysis was performed, with sample results shown in Fig. 40 for the patients previously discussed in Fig. 35. In Fig. 37, solid lines denote the mean error in each of the feedback signals over the time between BP cuff measurements (i.e. $\underset{k_p \le k < k_{p-1}}{\text{mean}} (\hat{u}_i - u_i)$, where k_p and $k_{p\text{-}1}$ represent the current and previous time steps at which BP cuff data was taken), ○ and x points indicate the maximum and minimum prediction errors at a single time points during each period, and dashed lines represent the expected standard deviation in feedback signals, approximated by the mean of corresponding diagonal terms in the error covariance matrix.

Among the training data set of 20 patients, it was observed that large but short duration errors were not strongly correlated with BP fluctuations. However, sustained positive error (predicted feedback magnitude larger than measured feedback magnitude, or "underperforming" expectations) in one or more feedback signals was observed preceding decompensation events. For example, for Patient 1, who had little variation in BP cuff measurements, mean feedback error was very close to zero; what error was present was also largely negative, implying stronger autoregulatory response than predicted by the model, and small relative to the expected range of deviation obtained from the EKF. In contrast, for Patient 2, who experienced large BP drops early in the session, feedback error was consistently positive and nearly a full standard deviation above that predicted by the estimator throughout the first two hours of hemodialysis.

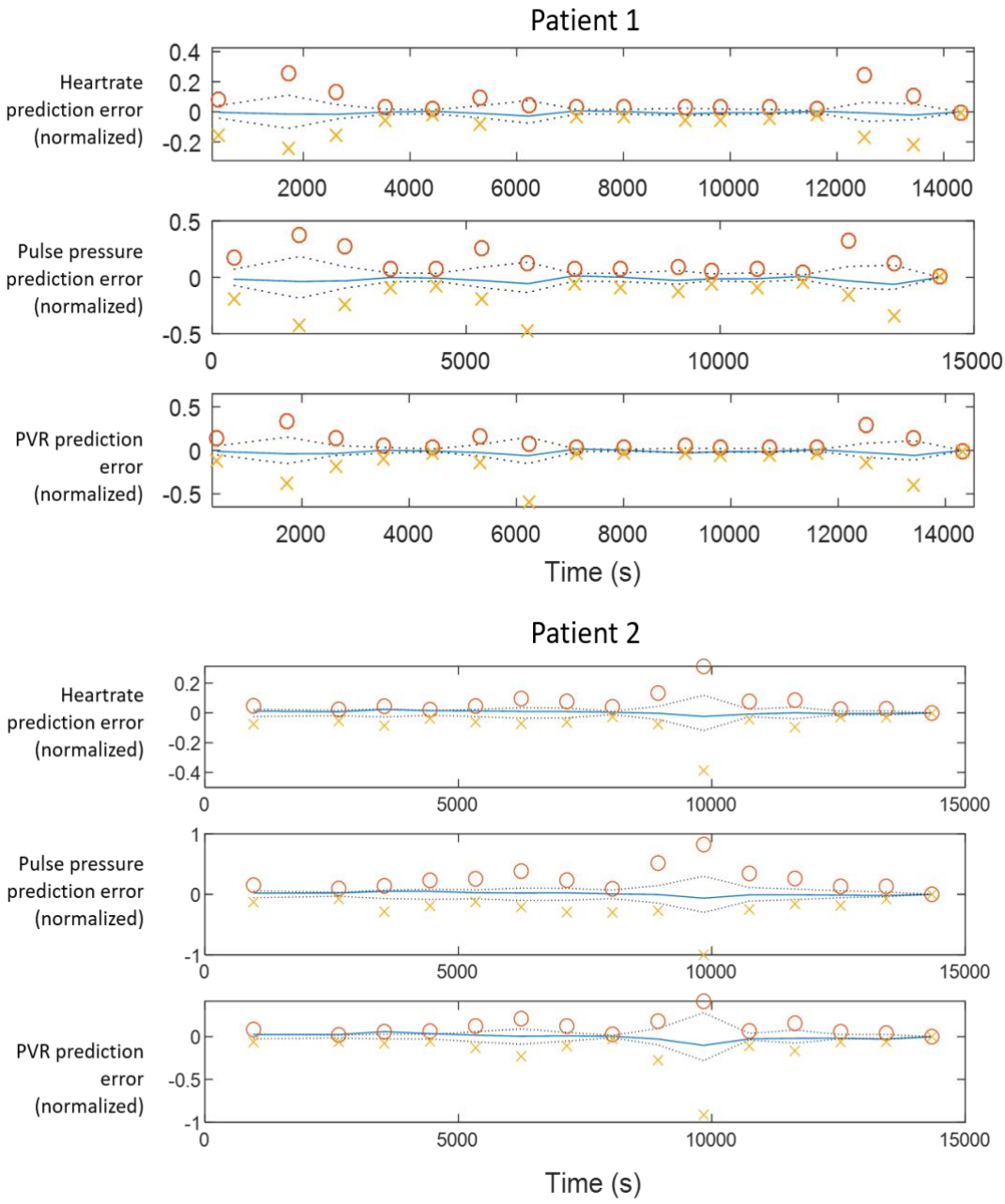

Fig. 38 For patients from Fig. 31, comparison of normalized prediction error (solid lines) for the three feedback signals in the dynamic BP model, averaged over time periods between BP cuff measurements, compared to worst case single time point prediction errors (◯: maximum, x: minimum) and approximate modeled standard deviation of those signals, as obtained from the EKF error covariance matrix. For Patient 1, error is small relative to anticipated deviation and tends negative (predicted response less than observed), while for Patient 2, who experienced large drops in BP, error tended positive (measured feedback lagging predicted levels) by nearly a full standard deviation.

7.6. Decompensation Prediction

Based on qualitative observations in Sections 7.4 and 7.5, decompensation prediction criteria were pursued based on thresholds for peripheral vascular resistance, mean feedback signal error, and time duration exceeding threshold values. A crude brute force evaluation of candidate thresholds and duration was performed on the 20 patient training set, to maximize the product of sensitivity and specificity in predicting decompensation. Decompensation was formally defined as a BP reduction >25% from baseline.

Best performance was found obtained for thresholds of pVR exceeding 165% of its initial value and mean feedback error exceeding 75% of predicted standard deviation, for a duration of 90 seconds. Under these criteria, sensitivity to future decompensation was 100% and specificity was 88% for the training data set, and 100% and 84% for the full 50 patient sample. Fig. 41 shows a sample ROC for the full sample when varying pVR threshold, with feedback error and duration are fixed. Area under the curve was 0.904. On average, thresholds were exceeded 59 minutes prior to decompensation measurement with the BP cuff.

A sample progression as observed under this approach to decompensation prediction is shown in Fig. 42, for a patient experiencing decompensation among the validation data set. Inferred peripheral vascular was elevated in this patient almost immediately and remained elevated throughout the session. Prediction error for feedback signals likewise

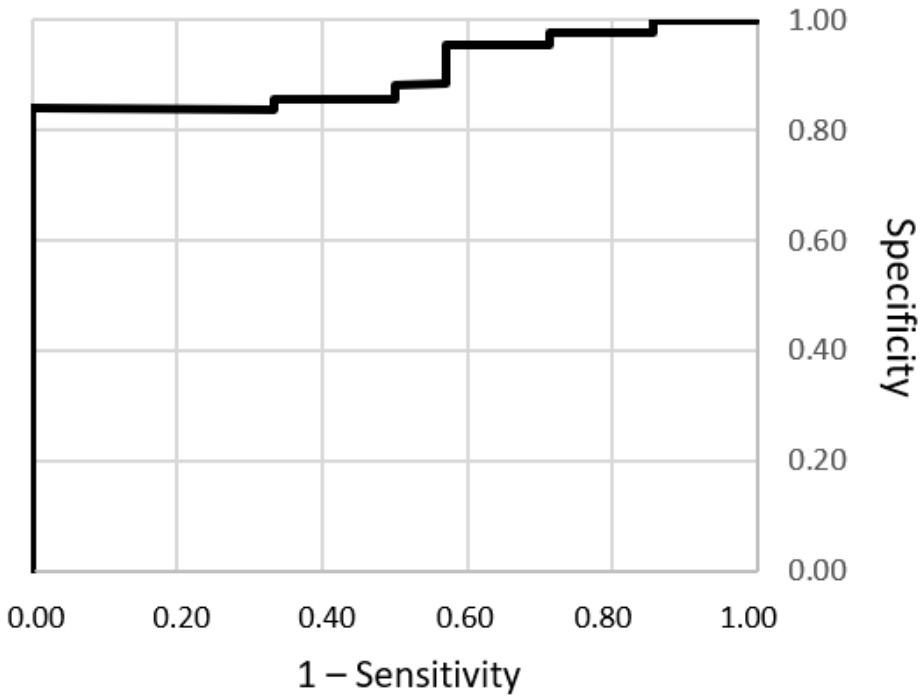

Fig. 39. ROC for prediction of decompensation (25% BP reduction from baseline) for varying peripheral vascular resistance thresholds accompanied by violation of feedback signal prediction error for at least 90 seconds.

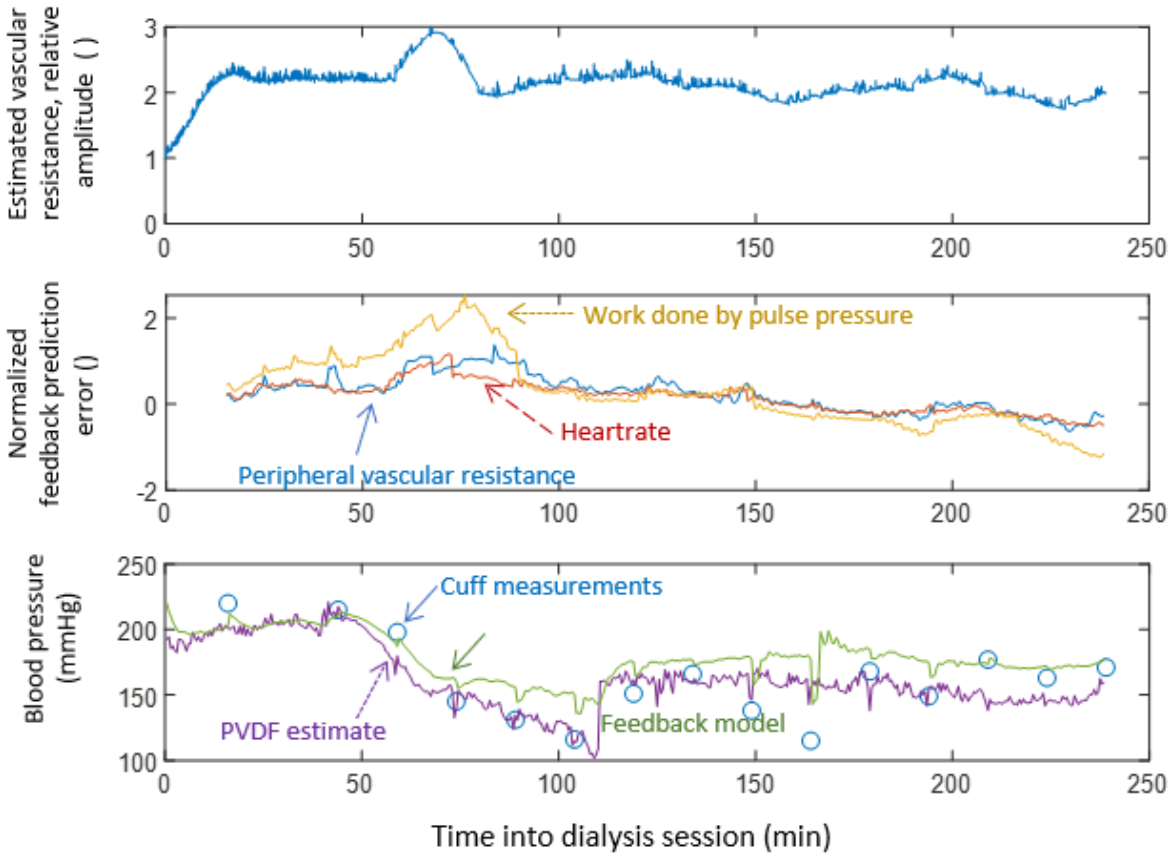

Fig. 40 (Top) Ratio of inferred peripheral vascular resistance to its initial value; (Middle) errors in measure feedback signals (positive values mean larger predicted value than measured), normalized by approximate standard deviation from EKF; (Bottom) BP trajectories, including values PVDF sensor as byproduct of pVR estimation and from the feedback model.

gradually increased during the first hour of hemodialysis, exceeding the error threshold criteria approximately 30 minutes into the session, at which point future decompensation is predicted to occur. In this case, weak mechanical work done to the sensor, perhaps interpretable as lagging pulse pressure, was the primary indicator of insufficient cardiovascular response to blood pressure changes, though additional deviation in both PVR and HR occurred approximately 60 minutes into the session. Formal decompensation criteria were not met until 89 minutes into the session, though BP decline had likely also begun to occur at approximately 60 minutes. The patient received a fluid bolus shortly thereafter, though if this was responsible for stabilizing BP, the estimator would suggest the bolus required tens of minutes to take effect.

7.7 Conclusions

This work uses a set of approximate measures of feedback signals important for blood pressure autoregulation over minute to hour timeframes to predict future decompensation in hemodialysis patients. Formally, BP drops >25% were predicted with good sensitivity and specificity using inferred changes in peripheral vascular resistance combined with prediction errors between anticipated magnitude of autoregulatory feedback signals and their measured values, as generated by a comparatively simple hemodynamic and autoregulatory dynamics model. Parameter identification and state estimation were performed concurrently on the model using an extended Kalman filter. Results are limited by lack of gold standard physiological data in the hemodialysis setting to better validate measurement accuracy, model structure, and physiological interpretations. However, relative success in decompensation prediction may suggest importance of capturing relative delay and interaction between feedback phenomena at an individually-identified level to predict hemodynamic decompensation events.

Results of this study to date are limited by relative rareness of quantifiable BP decompensation (as opposed to diagnosis based on symptoms or subjective observations) and reliance on substantial qualitative interpretation as gold standard measures of phenomena used in modeling are not available in the hemodialysis setting. As noted at their introduction, feedback measures are not individually validated in humans, and much support for their relevance remains subjective. Furthermore, dynamic models used to represent feedback dynamics are knowingly simplistic relative to real physiology. Even then, the large number of variables substantially limits trust in individual identified parameters, though outputs and system states seem to be reasonably predictable.

Nonetheless, the observed relationships between trends in model and estimator outputs and BP behavior for hemodialysis patients suggests to us that there is potential utility in the framework of control system analysis to the hemodynamic decompensation problem. We would interpret key features of the approach being the ability to adapt dynamics to individuals and thus account for variation and interconnectedness in relative timing of physiological phenomena. Differing delays in different signals for different individuals, in particular, can be hard to capture with other statistical methods. Future work will apply these methods to patients with more comprehensive physiological monitors, such as arterial lines, and on larger patient populations.

Chapter 8 Conclusion

Research objective 1: Assess peripheral artery behavior using non-invasive sensing methods

The candidate proposed a technique for tracking changes in vascular tone by combining a photo plethysmography sensor with an adjacent compliant piezoelectric polymer pressure sensor (polyvinylidene fluoride). In chapter 3, a simple local model for viscoelastic dynamic behavior of the underlying artery and surrounding tissue was generated and coupled to the piezoelectric/PPG sensor model, from which variations in relative amplitude and hysteresis between the piezoelectric and PPG signals were found to show strong correlations with invasively measured systemic vascular resistance data in animal subjects (swine).

The candidate then proposed an estimator based on the extended Kalman filter and the local nonlinear artery model in chapter 4. This Kalman filter method performs system identification and tracking the radius of peripheral arteries as well as blood pressure. In proof-of-concept testing on a swine test subject, local vascular resistance calculated from arterial radius estimates at the ring location showed good agreement with overall systemic vascular resistance, while capturing more roughly other features of local cardiovascular behavior. Further validation is performed with ultrasound measurements of wrist arterial radius while measurements with compliant sensors are taken. The radius of the artery is estimated by an edge-finding imaging processing algorithm to compensate for low ultrasound resolution, which shows reasonable accuracy of radius estimation from extended Kalman filter algorithms over long-term vascular tone changes.

Additionally, in chapter 5, a 2-D local model for arterial blood pressure, volumetric flow rate and artery radius with a varying outside cuff pressure was proposed. This model incorporates limited longitudinal behavior with peripheral arterial contraction dynamics beneath the PVDF/PPG sensor assembly to interpret variations in sensor signal behavior at varying applied external pressure. The experimental and modeled output from which variations in relative

amplitude of the signals are found shows strong correlation with invasively measured systemic vascular resistance (SVR) data in the swine subject.

Research objective 2: Identify systemic hemodynamic with respect to peripheral vascular resistance

In chapter 6, the candidate introduced a new systemic hemodynamic model, combining vascular resistance with heart rate, which may provide substantial insight into cardiovascular response to clinical interventions. This work attempted to better understand how estimated changes in local peripheral arterial radius obtained from wearable sensors relate to dynamic compensation in the full cardiovascular system. In this model, two compensatory mechanisms, heartrate and inferred vascular resistance, were monitored while a swine test subject underwent a series of experimental interventions, including various vasopressor infusions and controlled hemorrhage. Linear, empirical dynamic models for feedback and mean arterial pressure responses were identified, then assessed for reliability over repeated interventions. Changes in apparent dynamics after hemorrhage are observed and examined in terms of dynamic system stability. Significant results include the ability to reproduce oscillatory trajectories that appear to arise from different timescales of response to medication, and identifiable changes in the system "plant," i.e. blood pressure response to regulatory mechanisms, after hemorrhage.

Research objective 3: Predict hemodynamic decompensation with the systemic model

The candidate proposed using multiple criteria, drawn from local EKF estimations and systemic hemodynamic model, to predict decompensation, defined for these purposes as a BP reduction >25% from baseline. Human test data had been primarily collected from hemodialysis test subjects with a pulse plethysmograph and the compliant piezoelectric polymer (PVDF) worn on adjacent fingers. In addition to wearable sensor information, conventional cuff blood pressure (BP) was recorded approximately every 15 minutes. Tests were done to 110 hemodialysis patients in the inpatient dialysis unit at the University of Michigan Hospital, from which 91 complete data sets were successfully collected. Preliminary results show that under criteria based on peripheral vascular resistance increase and feedback model error, sensitivity to future decompensation was 100% and

specificity was 88% for the training data set, and 100% and 84% for the entire first 50 patients in the sample.

Future work

The candidate's techniques for tracking changes in vascular resistance by combining photo plethysmography sensor with compliant piezoelectric polymer pressure sensor may not only be used for non-invasive wearable devices, but also for invasive catherization. The candidate has developed an architecture that can extract high bandwidth measurements of blood volume fluctuations by reflectance fiber-based PPG methods and of pressure fluctuations from a piezoelectric polymer catheter coating. By using similar metrics to those used for SVR estimation in first research objectives, cerebral vascular resistance (CVR) is estimated to further calculate the cerebral blood flow. The estimated blood flow shows strong correlation with trans-cranial Doppler and laser Doppler flowmeter measurements on swine subjects.

For enhancing wearable sensing technology, the 2-D local artery and tissue model with a varying outside cuff pressure may eventually increase the accuracy of systolic and diastolic blood pressure measurements. More importantly, changes in sensor response to external pressure variation may allow changes in arterial properties (elasticity parameters, radius) in response to medical interventions to be inferred. The candidate's wearable sensor can be also used to assess other cardiovascular system characters, such as dynamic arterial elastance. Preliminary results suggest that both the piezoelectric and plethysmography sensor could be able to access the respiratory changes of blood pressure and cardiac flow. Non-invasive arterial elastance measurements agree with invasive catheterization method during norepinephrine infusions on swine subject.

A final future application of this sensor design is for blood pressure waveform analysis, using more detail information from piezoelectrical sensor. One recent study in the candidate's group uses waveform features from the sensor's signals to estimate absolutely values of systemic vascular resistance and blood pressure. A modest accuracy, competitive with prior literature results, is achieved on human subjects in cardiac catheterization lab.

References

[1] Kasaoka, Shunji. "Evolved role of the cardiovascular intensive care unit (CICU)." Journal of intensive care 5, no. 1 (2017): 72.

[2] M. Astiz, E. Tilly, E. Rackow and M. Weil, "Peripheral vascular tone in sepsis," Chest, vol. 99, no. 5, pp. 1072-1075, 1991.

[3] J. Siegel, M. Greenspan and L. Del Guercio, "Abnormal vascular tone, defective oxygen transport, and myocardial failure in human septic shock," Annals of Surgery, vol. 165, no. 4, pp. 504-517, 1967.

[4] A. Rachev, "Remodeling of arteries in response to changes in their mechanical environment," in Biomechanics of Soft Tissue in Cardiovascular Systems, Springer, 2014, pp. 218-272.

[5] O. Godje, K. Hoke, P. Lamm, C. Schmitz, C. Thiel, M. Weinert and B. Reichert, "Continuous, less invasive, hemodynamic monitoring in intensive care after cardiac surgery," Thoracic and Cardiovascular Surgeon, vol. 46, no. 4, pp. 242-249, 1998.

[6] B. Straver, M. Roggekamp, P. de Vries and P. der Wee, "Systemic vascular resistance in intradialytic hypotension determined by means of impedance cardiography," Blood Purification, vol. 16, pp. 281-289, 1998.

[7] G. Gamble, J. Zorn, G. Sanders, S. MacMahon and N. Sharpe, "Estimation of arterial stiffness, compliance, and distensibility from M-mode ultrasound and measurements of the common carotid artery," Stroke, vol. 25, no. 1, pp. 11-16, 1994.

[8] R. Stadler, W. Karl and R. Lees, "New methods for arterial diameter measurement from B-mode images," Ultrasound in Medicine and Biology, vol. 22, no. 1, pp. 25-34, 1996.

[9] A. E. Abbas, F. D. Fortuin, B. Patel, C. A. Moreno, N. B. Schiller and S. J. Lester, "Noninvasive measurement of systemic vascular resistance using Doppler echocardiography," Journal of the American Society of Echocardiography, vol. 17, no. 8, pp. 834-838, 2004.

[10] N. Fazeli and J. O. Hahn, "Estimation of cardiac output and peripheral resistance using square-wave-apaproximated aortic flow signal," Frontiers in Physiology, vol. 3, pp. 58-67, 2012.

[11] J.-J. Wang, J. A. Flewitt, N. G. Shrive, K. H. Parker and J. V. Tyberg, "Waves propagating on a windkessel: relation of arterial and venous windkessels to systemic vascular resistance," American Journal of Physiology, vol. 290, no. 1, pp. H154-H162, 2006.

[12] J. Narula, U. Kiran, S. Chouhan, S. Ramakrishnan and A. Chowdhary, "Electrical cardiometry in patients undergoing cardiac cathererisation," International Journal of Perioperative Ultrasound and Applied Technologies, vol. 2, no. 3, pp. 102-107, 2013.

[13] A. Tahvanainen, J. Koskela, M. Leskinen, E. Ilveskoski, K. Norhaussen, M. Kahonen, T. Koobi, J. Mustonen and I. Porsti, "Reduced systemic vascular resistance in healthy volunteers with presyncopal symptoms during a nitrate-stimulated tilt-table test," British Journal of Clinical Pharmacology, vol. 71, no. 1, pp. 41-51, 2011.

[14] V. Sharma, A. Singh, B. Kansara and A. Karlekar, "Comparison of transthoracic electrical bioimpedance cardiac output measurement with thermodilution method in post-coronary artery bypasses graft patients," Annals of Cardiac Anaesthesia, vol. 14, no. 2, pp. 104-110, 2011.

[15] R. B. Schnabel, A. Schulz, P. S. Wild, C. R. Sinning, S. Wilde, M. Eleftheriadis, S. Herkenhoff, T. Zeller, E. Lubos, K. J. Lackner, A. Warmnoltz, T. Gori, S. Blankenberg and T. Munzel, "Noninvasive vascular

function measurement in the community," Circulation: Cardiovascular Imaging, vol. July, pp. 371-380, 2011.

[16] A. Scholze, A. Burkurt, K. Mardanzai, S. Suvd-Erdene, M. Hausberg, W. Zidek and M. Tepel, "Increased arterial vascular tone during the night in patients with esential hypotension," Journal of Human Hypertension, vol. 21, pp. 60-67, 2007.

[17] T. Morise, M. Horita, N. Honda, K. Masuura, I. Kitagawa, R. Shinzato, Y. Hoshiba, H. Masuya and N. Takekoshi, "Noninvasive, continuous evaluation of peripheral vascular resistance in humans," Hypertension Research, vol. 23, pp. 15-19, 2000.

[18] Q. Y. Lee, S. J. Redmond, G. S. Chan, P. M. Middleton, E. Steel, P. Malouf, C. Critoph, G. Flynn, E. O'Lone and N. H. Lovell, "Estimation of cardiac output and systemic vascular resistance using a multivariate regression model with features selected from the finger photoplethysmogram and routine cardiovascular measurements," Biomedical Engineering Online, vol. 12, no. 19, pp. 1-16, 2013.

[19] Y.-L. Zheng, B. P. Yan, Y.-T. Zhang and C. C. Poon, "Noninvasive characterization of vascular tone by model-based system identification in healthy and heart failure patients," Annals of Biomedical Engineering, vol. 10, p. 10.1067, 2015.

[20] H. Ishihara and M. Tsutui, "Impact of changes in systemic vascular resistance on a novel non-invasive continuous cardiac ouput measurement system based on pulse wave transit time: a report of two cases," Journal of Clinical Monitoring and Computing, vol. 28, pp. 423-427, 2014.

[21] B. Haslem, A. Gordhandas, C. Ricciardi, T. Heldt and G. Veerghese, "Relating noninvasive cardiac output and total peripheral resistance estimates to phsyical activity in an ambulatory setting," Computational Physiology, Vols. SS-11-04, pp. 27-331, 2011.

[22] S. Sur and S. Ghatak, "An inexpensive arterial pressure wave sensor and its application in different physiological conditions," arxiv.org, 2005.

[23] Y.-Y. Chiu, W.-Y. Lin, H.-Y. Wang, S.-B. Huan and M.-H. Wu, "Development of a piezoelectric polyvinylidene fluoride (PVDF) polymer-based sensor patch for simultaneou heartbeat and respiration monitoring," Sensors and Actuators A: Physical, vol. 189, pp. 328-334, 2013.

[24] C. Dagdeviren, Y. Su, P. Joe, R. Yona, Y. K. Y.-S. Liu, Y. Huang, A. H. J. Damadoran and J. Rogers, "Conformable amplified lead zirconate titanate sensors with enhanced piezoelectric response for cutaneous pressure monitoring," Nature Communications, 2014.

[25] S. Gong, W. Schwaib, Y. Wang, Y. Chen, Y. Tang, J. Si, B. Shirnzadeh and W. Cheng, "A wearable and highly sensitive pressure sensor with ultrathin gold nanowires," Nature Communications, vol. 5, p. 10.1038, 2013.

[26] H.-J. Tseng, W.-C. Tian and W.-J. Wu, "Flexible PZT thin film tactile sensor for biomedical monitoring," Sensors, vol. 13, pp. 5478-5492, 2013.

[27] Bär, Karl-Jürgen (2015-06-24). "Cardiac Autonomic Dysfunction in Patients with Schizophrenia and Their Healthy Relatives – A Small Review". Frontiers in Neurology. Frontiers Media SA. 6. doi:10.3389/fneur.2015.00139. ISSN 1664-2295. PMC 4478389. PMID 26157417.

[28] Fountain, John H. (5 May 2019). "Physiology, Renin-Angiotensin System". NCBI. NIH. Retrieved 9 May 2019.

[29] Mukkamala, R., Hahn, J.-O., Inan, O.T., Mestha, L.K., Kim, C.-S., Töreyin, H., and Kyal, S. "Toward ubiquitous blood pressure monitoring via pulse transit time: theory and practice." IEEE Transactions on Biomedical Engineering 62:8 (2015): 1879-1901

[30] Lau, K.D. and Figueroa, A.F. "Simulation of short-term pressure regulation during the tilt test in a coupled 3D–0D closed-loop model of the circulation." Biomechanics and modeling in mechanobiology 14:4 (2015): 915-929.

[31] McLoone, V. Modeling of Long and Short Term Blood Pressure Control Systems, Ph.D. Thesis, National University of Ireland Maynooth (2014).

[32] Ataee, P., Hahn, J.-O., and Dumont, G.A., “Noninvasive subject-specific monitoring of autonomic cardiac regulation,” IEEE Transactions on Biomedical Engineering 61:4 (2014): 1196-1207.

[33] L. Gabutti, M. Machacek, C. Marone and P. Ferrari, "Predicting intradialytic hypotension from experience, statistical models, and artificial neural networks," Journal of Nephrology, vol. 18, no. 4, pp. 409-416, 2005.

[34] R. Mendes, S. Santos, D. Dorigo, G. Mansoor, S. Crowley, W. White and A. Peixoto, "The use of peridialysis blood pressure and intradialytic blood pressure changes in teh prediction of interdialytic blood pressur in hemodialysis patients," Blood Pressure Monitoring, vol. 8, no. 6, pp. 243-248, 2003.

[35] K. Solem, B. Olde and L. Sornmo, "Predition of intradialytic hypotension using photoplethysmography," IEEE Transactions on Biomdical Engineering, vol. 57, no. 7, pp. 1611-1619, 2010.

[36] F. Sandberg, R. Bailon, D. Hernando, P. Laguna, J. Martinez, K. Solem and L. Sornmo, "Prediction of intradialytic hypotension using PPG and ECG," in Computing in Cardiology, Zaragoza, Spain, 2013.

[37] C.-J. Lin, C.-Y. Chen, P.-C. We, C.-F. Pan, H.-M. Shih, M. Huang, L.-H. Chou, J.-S. Tang and C.-J. Wu, "Intelligent system to predict intradialytic hypotension in chronic hemodialysis," Journal of Formosan Medical Association, vol. 117, no. 10, pp. 888-893, 2018.

[38] V. Chan, L. Chan and D. Chow, "Oxygen saturation and heart rate variations as predictors of intradialytic hypotension," Nephrology Nursing Journal, vol. 45, no. 1, pp. 53-61, 2018.

[39] Wang, Lu, Sardar Ansari, Daniel Slavin, Kevin Ward, Kayvan Najarian, and Kenn R. Oldham. "Non-invasive vascular resistance monitoring with a piezoelectric sensor and photoplethysmogram." Sensors and Actuators A: Physical 263 (2017): 198-208.

[40] Wang, Lu, Sardar Ansari, Kevin R. Ward, Kayvan Najarian, and Kenn R. Oldham. "Identification of Compensatory Arterial Dynamics in Swine Using a Non-Invasive Sensor for Local Vascular Resistance." 2017 American Control Conference (ACC), 2017

[41] Wang, Lu, Sardar Ansari, Kevin R. Ward, Kayvan Najarian, and Kenn R. Oldham. ”Modeling peripheral artery behavior beneath a non-invasive wearable sensor subject to varying outside pressure." In *ASME 2019 Dynamic Systems and Control Conference*. American Society of Mechanical Engineers Digital Collection, 2019.

[42] Bergel, D. H. "The static elastic properties of the arterial wall." The Journal of physiology 156.3 (1961): 445-457.

[43] Lopes-Berkas, Vanessa C, and Michael A Jorgenson. “Measurement of peripheral arterial vasculature in domestic Yorkshire swine by using quantitative vascular angiography.” Journal of the American Association for Laboratory Animal Science : JAALAS vol. 50,5 (2011): 628-34.

[44] Nolan, D. R., and J. P. McGarry. "On the compressibility of arterial tissue." Annals of biomedical engineering 44.4 (2016): 993-1007.

[45] Cutnell, John & Johnson, Kenneth. Physics, Fourth Edition. Wiley, 1998: 308.

[46] Wang, Lu, Sardar Ansari, Kevin R. Ward, Kayvan Najarian, and Kenn R. Oldham. " Estimation of peripheral artery radius using non-invasive sensors and Kalman filtering of local dynamics ." In ASME 2018 Dynamic Systems and Control Conference. American Society of Mechanical Engineers Digital Collection, 2018.

[47] Wang, Lu, Sardar Ansari, Kevin R. Ward, Kayvan Najarian, and Kenn R. Oldham. “Decompensation Prediction in Hemodialysis by a Feedback Model as Identified by Miniature Wearable Sensors” 2019 IEEE/ASME International Conference on Advanced Intelligent Mechatronics (AIM) , 2019